Energy Conversion and Management 348 (2026) 120666

Contents lists available at ScienceDirect

Energy Conversion and Management

journal homepage: www.elsevier.com/locate/enconman

Research Paper

Modelling of borehole thermal energy storages: A g-function approach with a novel load aggregation scheme

Angela Valeria Miceli *, Alessandro Buscemi, Stefania Guarino, Marco Beccali, Valerio Lo Brano

Department of Engineering, University of Palermo, Viale delle Scienze, Palermo, Italy

ARTICLE INFO

Keywords:
Borehole Thermal Energy Storage
G-functions
Load Aggregation Algorithm
Finite Element Modelling
Python model

ABSTRACT

Borehole Thermal Energy Storage systems can play a pivotal role in enhancing the energy efficiency of building heating, promoting the widespread adoption of heat pumps and solar thermal solutions especially at district-level. In this paper, a novel Python-based model for the analysis of these renewable systems is proposed employing a g-function approach and introducing a new thermal load aggregation scheme to enable accurate and efficient numerical simulations. The proposed model was applied to assess the operation of a recently constructed pilot-scale seasonal thermal storage at the University of Palermo campus, thus demonstrating the feasibility of deploying this technology for building heating in the Mediterranean region. For this case study, multiple g-functions were generated using both the Python *pygfunction* library and finite element models developed in COMSOL Multiphysics®, allowing investigation of how borehole hydraulic connections, undisturbed thermal profiles, soil thermophysical properties, and storage surface insulation conditions influence the thermal response of the borehole thermal energy storage. The results indicate that the novel load aggregation scheme markedly reduces the errors encountered by conventional algorithms, particularly during the sharp thermal load variations between charging and discharging phases. Moreover, simulations conducted with the new code confirmed a seasonal efficiency of approximately 70 % for the Palermo storage and revealed that perfect surface insulation could raise its thermal level by about 4 °C. The new modelling framework also paves the way for a future Digital Twin that will enable real-time optimization of charge/discharge cycles.

1. Introduction

The global transition to renewable energy is crucial to mitigate climate change and reduce greenhouse gas emissions, which have reached record levels [1]. To achieve the 1.5 °C target by 2050, the expansion of renewable energy, electrification and energy efficiency must accelerate [2]. Buildings, which account for 17.5 % of global emissions [3], are a critical focus area, with over 50 % of their energy consumption dedicated to heating and hot water production [4]. Heat pumps will play a key role in decarbonization, with their installed capacity expected to triple by 2030 [5]. In this context, a promising approach to improve the efficiency of heat pumps is integrating them with Seasonal Thermal Energy Storage (STES) systems [6], which can overcome the mismatch between demand and supply of solar energy across seasons [7]. STES can also be integrated at district level with power-to-heat technologies for smarter management of excess power produced by renewable systems [8]. Among the four main types of STES systems [9], Borehole Thermal Energy Storage (BTES) systems stand out as one of the most economically viable storage methods [10]. These systems enable large-scale seasonal energy storage with high efficiency and minimal heat losses [10].

Similarly to a Ground Source Heat Pump (GSHP) system, a BTES system consists of a set of Borehole Heat Exchangers (BHEs) [10]. Within each borehole, either a U-shaped or double U-shaped pipe is installed and embedded in a special cement mixture (grout). Through these BHEs, heat exchange occurs between the soil and the heat transfer fluid [7], typically water or a mixture of water and glycol. However, while GSHPs extract or inject heat from the soil, BTES systems are designed to actively store and retrieve thermal energy over seasonal cycles. As a result, the annual cycles of thermal charging and discharging of the soil progressively brings the mean soil temperature to a pseudo-stationary regime state after approximately five years [11]. This distinction leads to significant differences in their design and operation [10]:

* Corresponding author.
E-mail address: angelavaleria.miceli@unipa.it (A.V. Miceli).

https://doi.org/10.1016/j.enconman.2025.120666
Received 9 April 2025; Received in revised form 1 August 2025; Accepted 12 October 2025
Available online 21 October 2025

Nomenclature

A	area [m^2]
a_1	coefficient related to heat loss expression [$W \cdot m^{-2} \cdot K^{-1}$)]
a_2	coefficient related to heat loss expression [$W \cdot m^{-2} \cdot K^{-2}$)]
b_0	shape parameter specific to the collector
b_1	shape parameter specific to the collector
B	average distance between boreholes [m]
c_p	specific heat [$J \cdot kg^{-1} \cdot K^{-1}$]
C_p	volumetric heat capacity [$J \cdot m^{-3} \cdot K^{-1}$]
C	constant depending on the geometry of the borehole
D_p	pipe diameter [m]
D	buried depth of the boreholes [m]
E	thermal energy [MWh]
g	g-function
G_{tot}	global solar irradiance on the collector plane [$W \cdot m^{-2}$]
h	convective heat transfer coefficient [$K \cdot m \cdot W^{-1}$]
H	length of the BHE [m]
H_{POA}	Radiation on the Plane of Array [$kWh \cdot m^2$]
IAM	Incidence Angle Modifier
L	length [m]
$\dot{m}$	mass flow rate [$kg \cdot s^{-1}$]
n_{FPC}	number of Flat-Plate Collectors
n_p	number of tubes in each borehole cross section
$\dot{Q}_{sol,net}$	rate of energy production [W]
$\dot{Q}$	internal source term [W·m-3]
$\overline{q}$	heat flux density [$W \cdot m^{-2}$]
$\overline{q}_h$	endogenous heat flux for continental area [$W \cdot m^{-2}$]
$\dot{q}_{fs}$	thermal power exchanged per unit length of pipe [$W \cdot m^{-1}$]
r	radius [m]
R	equivalent thermal resistance [$K \cdot m \cdot W^{-1}$]
Re	Reynolds number
t	time [s]
t_s	characteristic time [s]
T	temperature [°C]
$\overline{T}$	average temperature [°C]
T_b^*	average effective borehole wall temperature [°C]
T_0	average undisturbed soil temperature [°C]
x	curvilinear abscissa along the development of the pipe

Greek letters

α_s	thermal diffusivity of soil [$m^2 \cdot s^{-1}$]
η	efficiency
θ	incidence angle for beam radiation
λ	thermal conductivity [$W \cdot m^{-1} \cdot K^{-1}$]
ρ	density [$kg \cdot m^{-3}$]

Subscripts

air	air
b	borehole
conv	convective
clay	clay
extracted	extracted
f	fluid
field	field
fp	fluid-pipe
FPC	Flat-Plate Collector
g	grout
i	inner
in	inlet
injected	injected
ins	insulating layer
multipole	calculated with multipole method
o	outer
out	outlet
p	pipe
ref	reference
s	soil
t	total

Acronyms

AE	Absolute Error
BHE	Borehole Heat Exchanger
BTES	Borehole Thermal Energy Storage
DST	Duct Ground Heat Storage
FE	Finite Element
FEM	Finite Element Method
FLS	Finite Linear Source
GAA	Geometric Aggregation Algorithm
GAEC	Geometric Aggregation Algorithm with Error Control
GSHP	Ground Source Heat Pump
MAE	Mean Absolute Error
MIFT	Mixed Inlet Fluid Temperature
PDE	Partial Differential Equation
RGAA	Restricted Geometric Aggregation Algorithm
SMARTEP	Sustainable Model And Renewable Thinking Energy Parking
STES	Seasonal Thermal Energy Storage
UHTR	Uniform Heat Transfer Rate

Glossary of Developed Models

FE UHTR	Simplified FE model for UHTR conditions
FE MIFT 1	Simplified FE model for MIFT conditions
FE MIFT 2	More complex FE model for UHTR conditions
Condition A	Absence of the insulation layer at the top surface
Condition B	Presence of the insulation layer at the top surface
Condition C	Adiabatic condition at the top surface
Scenario S1	Initial condition and physical properties are assumed to be constant in time and space
Scenario S2	Thermal profile and physical properties are assumed to be variable with depth
Py-MIFT	Model MIFT developed in Python
Py-UHTR	Model UHTR developed in Python

- Boreholes Configuration: BTES systems typically feature shorter borehole lengths and distances to promote thermal interaction between the exchangers and reduce heat losses to more distant soil volume, whereas traditional GSHP systems reach deeper and stable temperature zones.
- System Layout: the exchangers in a BTES system are usually connected either in series or in parallel, with flow direction changing based on charging or discharging phase, while GSHP systems predominantly use parallel configurations.
- Thermal Insulation: since the exchangers of a BTES system are shorter, the influence of external atmospheric conditions is more pronounced. To minimize heat losses and mitigate the effect of atmospheric variations on soil temperature, a thermal insulation layer is often applied to the upper surface—an aspect not required in GSHP systems.

BTES systems are predominantly present in cold climates [12], where they significantly improve the efficiency of Heating, Ventilating and Air Conditioning systems [13]. A study on Nordic regions [14]

demonstrated that a hybrid energy system with BTES can cover up to 88 % of heating demand and reduce CO_2 emissions by up to 66 %, highlighting its efficiency in cold climates. However, the potential of BTES systems in milder climates, such as the Mediterranean region [15], has not yet been fully explored. Nevertheless, there is an increasing interest in the potential of BTES systems in these areas, with studies suggesting that they could be highly effective, as evidenced by proposed applications in locations such as Palermo [16] and southern Spain [17], where they could cover up to 70 % of heating demand with solar energy.

Despite their advantages, BTES systems are characterized by a higher degree of complexity in terms of design, installation, and operation compared to conventional GSHP systems [10]. This complexity extends to the numerical approaches used to study their operation, as existing approaches often struggle to fully capture their dynamic behaviour. The methods commonly employed to simulate GSHP systems rely on solving Partial Differential Equations (PDEs) that represent the energy balance of the system. These approaches can be broadly classified as follows:

1. Analytical solutions, such as the Finite Linear Source (FLS) [18] and the Cylindrical Heat Source [19] solutions, are efficient but rely on highly idealised assumptions and are often employed for highly idealised configurations. Recently, these solutions have been integrated into increasingly sophisticated hybrid numerical approaches [20]. However, there are still no analytical models that consider the series and parallel connections of BHEs in a BTES system.
2. Numerical models, including Finite Difference Method and Finite Element Method (FEM), offer greater accuracy by allowing for realistic consideration of complex three-dimensional layouts, varying thermophysical properties, and complex boundary and initial conditions [21]. However, their complexity and high computational cost hinder widespread adoption [22]. In addition, numerical models are difficult to integrate as stand-alone modules into energy simulation software such as TRNSYS [23], limiting their wider applicability.
3. Hybrid models, such as the Duct Ground Heat Storage (DST) model [24], combine analytical and numerical techniques to improve efficiency. The DST is implemented in a Type in TRNSYS [23], making it readily and widely available, but it has important limitations [25]: it assumes axisymmetric layouts and constant thermal resistance, and does not capture the short-term response of borehole heat exchangers.

A powerful alternative to traditional modelling approaches is the use of g-functions [26], which provide precomputed solutions for the thermal response of borehole fields characterised by the same geometric relationships of their elements (borehole diameters, distances, etc.) and values of the thermophysical properties of the soils. Unlike traditional numerical methods, g-functions do not solve PDEs directly but instead provide precomputed solutions that describe the thermal response of BHE fields. These functions enable fast and accurate dynamic simulations via convolution products [27] and advanced load aggregation techniques [28], making them particularly useful for parametric optimization and Digital Twin applications in BTES systems. In this context, recent models for the definition of g-functions, based on the analytical solution of FLS and implemented in the Python *pygfunction* library [29], also allow the consideration of series and parallel connections between BHEs [30]. However, their application to the analysis of BTES systems is still limited by the fact that these models do not consider the top insulating layer, the possibility that the thermophysical properties of the soil vary with depth, and the effect of the geothermal gradient.

To sum up, the literature analysis shows that there are no analytical or numerical models available today which are both rapidly developing and able to incorporate realistically all the characteristics peculiar to BTES systems.

This study therefore investigated the impact of key physical assumptions and boundary conditions on the dynamic thermal response of BTES systems, particularly the influence of soil properties variability and the presence of a top insulation layer. The case study focuses on a pilot BTES system at the University of Palermo [31], integrating solar thermal collectors and BTES to demonstrate the feasibility of seasonal thermal storage in warmer climates. In order to simulate the system's operation over successive thermal loading and unloading cycles, a new Python-based model was developed, integrating a g-function approach and a novel load aggregation algorithm. The new algorithm proposed in this work is based on the well-known geometric aggregation algorithm [32] but, for the first time, accounts for the effect of varying thermal loads on aggregation error. The g-functions of the studied BTES were obtained via both the *pygfunction* library and a three-dimensional FE multiphysics model developed in COMSOL Multyphisics® [33], enabling cross-validation of the two numerical approaches. Both models were calibrated using thermophysical parameters deduced from experimental-numerical analyses previously conducted on the pilot plant of Palermo [31]. To sum up, the main contributions of this work are:

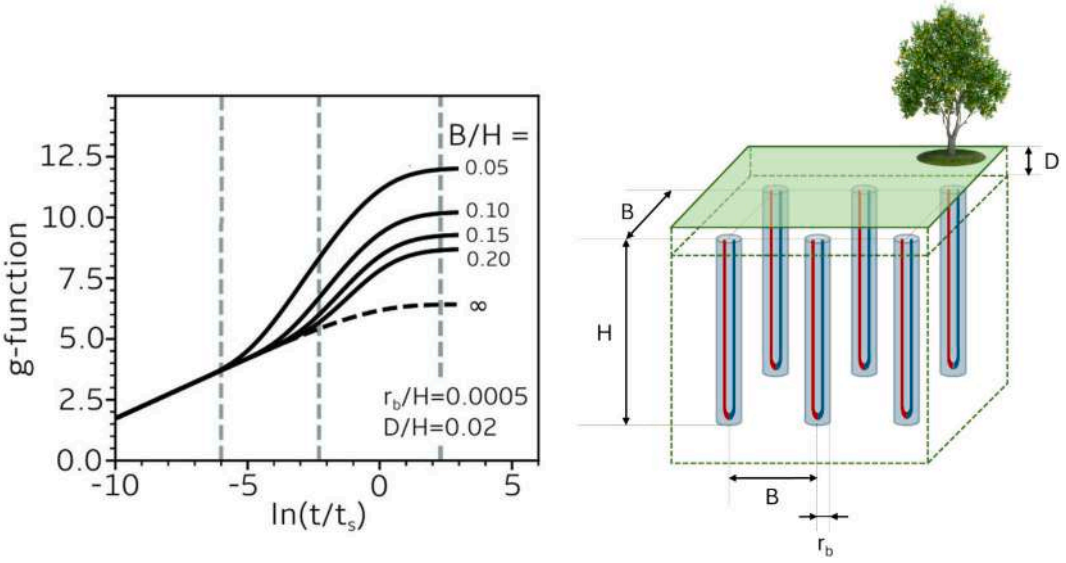

Fig. 1. g-functions for a 3 × 2 bore field, as shown on the right.

- A novel load aggregation scheme that dynamically adjusts to varying thermal loads, improving simulation accuracy.
- A new methodology to define the minimum calculation domain of the FE model by comparing the g-functions derived from *pygfunction* and FE simulations (cross-validation).
- Derivation of g-functions specific to the case study geometry, representative of a typical BTES configuration.
- Investigation of the effect of key physical assumptions, such as soil properties variability and the presence of top insulation, to enhance BTES performance predictions.
- Development of a new Python-based solar-assisted BTES model that uses g-functions as input and the new load aggregation scheme.

The model developed in this study will be utilised for the development of the Digital Twin of the Palermo BTES system, which will be crucial in establishing a real-time optimised control system for the pilot plant. This, in turn, will enhance the operational efficiency and long-term performance of the latter.

2. g-functions: Key concepts and applications

This section defines g-functions, explains their role in BTES system analysis, and discusses the boundary conditions that influence their application, with a focus on the impact of borehole arrangement and hydraulic configuration on thermal performance.

2.1. Definition

g-functions are time-dependent thermal response factors that describe how a borehole field reacts to heat exchange over time. Derived from analytical or numerical solutions to heat transfer equations, g-functions can be used to model the temperature evolution in BTES systems. By using g-functions, it is possible to simulate the thermal behaviour of these systems without repeatedly solving partial differential equations. This approach significantly reduces computational requirements while maintaining adequate accuracy in predicting the performance of the system. The use of g-function simplifies the design and optimization process, making it more efficient and less computationally demanding. A g-function can be considered representative of all borehole fields that have similar geometry and the same dimensionless ratios (r_b/H, B/H, D/H), where r_b [m] is the borehole radius, H [m] the borehole length, B [m] the boreholes spacing, D [m] the buried depth, regardless of the undisturbed temperature and the thermophysical properties of the soil. For example, Fig. 1 shows a graph with the calculated g-functions for a layout consisting of six probes arranged as shown in the figure.

The g-function [26] of a geothermal field describes the change over time in the average effective borehole wall temperature T_b^* [°C], considering a constant thermal heat flux $\dot{q}$ [W/m] (as seen in [34]):

$$g\left(\frac{t}{t_s};\frac{r_b}{H};\frac{B}{H};\frac{D}{H}\right) = \frac{T_b^*(t) - T_0}{\dot{q}}\cdot(2\cdot\pi\cdot\lambda_s) \tag{1}$$

where T_0 [°C] is the undisturbed soil temperature, λ_s [W/(m·K)] the thermal conductivity of the soil, r_b [m] the borehole radius,B [m] the average borehole to borehole spacing, D [m] the buried depth of the boreholes, H [m] the length of the exchangers, and t_s [s] a characteristic time defined as in [35]:

$$t_s = \frac{H^2}{9\cdot\alpha_s} \tag{2}$$

where α_s [m^2/s] is the thermal diffusivity of the soil.

2.2. Application in BTES systems

For BTES systems, the average fluid temperature $\overline{T}_f$ in the bore field can be correlated with the effective borehole wall temperature T_b^* through a relationship that can be expressed as follows [30]:

$$\overline{T}_f = T_b^* + R_{field}^*\cdot\dot{q} \tag{3}$$

where R_{field}^* [m·K·W^{-1}] is the effective thermal resistance of the bore field.

The arrangement of boreholes, whether in parallel or series configurations, has a significant impact on the effective thermal resistance of the bore field. When BHEs are hydraulically connected in parallel, as in Ground Source Heat Pumps, the effective thermal resistance of the system can be equated to the individual borehole resistance R_b. When considering geothermal fields where boreholes are arranged in both parallel and series configurations (e.g., in BHEs of BTES systems), the following equation (equivalent to the formulation proposed in [30]) can be utilised to determine the effective thermal resistance:

$$R_{field}^* = \frac{L_t}{2\cdot\dot{m}_{f,t}\cdot c_{pf}}\cdot\left[\frac{1+e^{-\left(\frac{L_t}{\dot{m}_{f,t}\cdot c_{pf}\cdot R_b}\right)}}{1-e^{-\left(\frac{L_t}{\dot{m}_{f,t}\cdot c_{pf}\cdot R_b}\right)}}\right] \tag{4}$$

where L_t [m] is the total length of the exchangers, $\dot{m}_{f,t}$ [kg·s^{-1}] the total circulating mass flow in BHEs, c_{pf} [J·kg^{-1}·K^{-1}] the specific heat of the fluid, and R_b [m·K·W^{-1}] the thermal resistance of the borehole. The derivation of the effective bore field thermal resistance for series-connected boreholes is provided in the Supplementary Information. It can be easily demonstrated from the above formula that as the mass flow in the field increases, the two values of the thermal resistance of the bore field R_{field}^* and the individual borehole R_b tend to converge, even in the case of both series and parallel-connected heat exchangers [30]:

$$\lim_{\dot{m}_{f,t}\to\infty} R_{field}^* = R_b \tag{5}$$

Thus, in the assessment of g-functions, two boundary conditions can be considered:

1. Uniform Heat Transfer Rate (UHTR): the heat extraction rate is uniformly distributed along the length of each borehole, maintaining constant values across all boreholes, while the average temperature along the length of each borehole varies and is non-uniform across the field. The condition delineated corresponds to the assumptions of the FLS analytical solution.
2. Mixed Inlet Fluid Temperature (MIFT): this condition allows for the consideration of series connections of BHEs, where the outlet temperature of one borehole becomes the inlet temperature of the next. Unlike the simplified UHTR condition, MIFT also captures the non-uniform flow distribution among boreholes, thereby providing a more accurate representation of typical BTES system configurations.

These will influence the output, particularly for high time values and fields with a large number of boreholes.

3. Methods

This section describes the multi-phase methodology used to analyse the performance of a solar-assisted BTES system. The process begins with input data collection, including BTES geometric and thermophysical parameters. The methodology involves the generation of g-functions using both Python (*pygfunction*) and FEM (COMSOL) approaches,

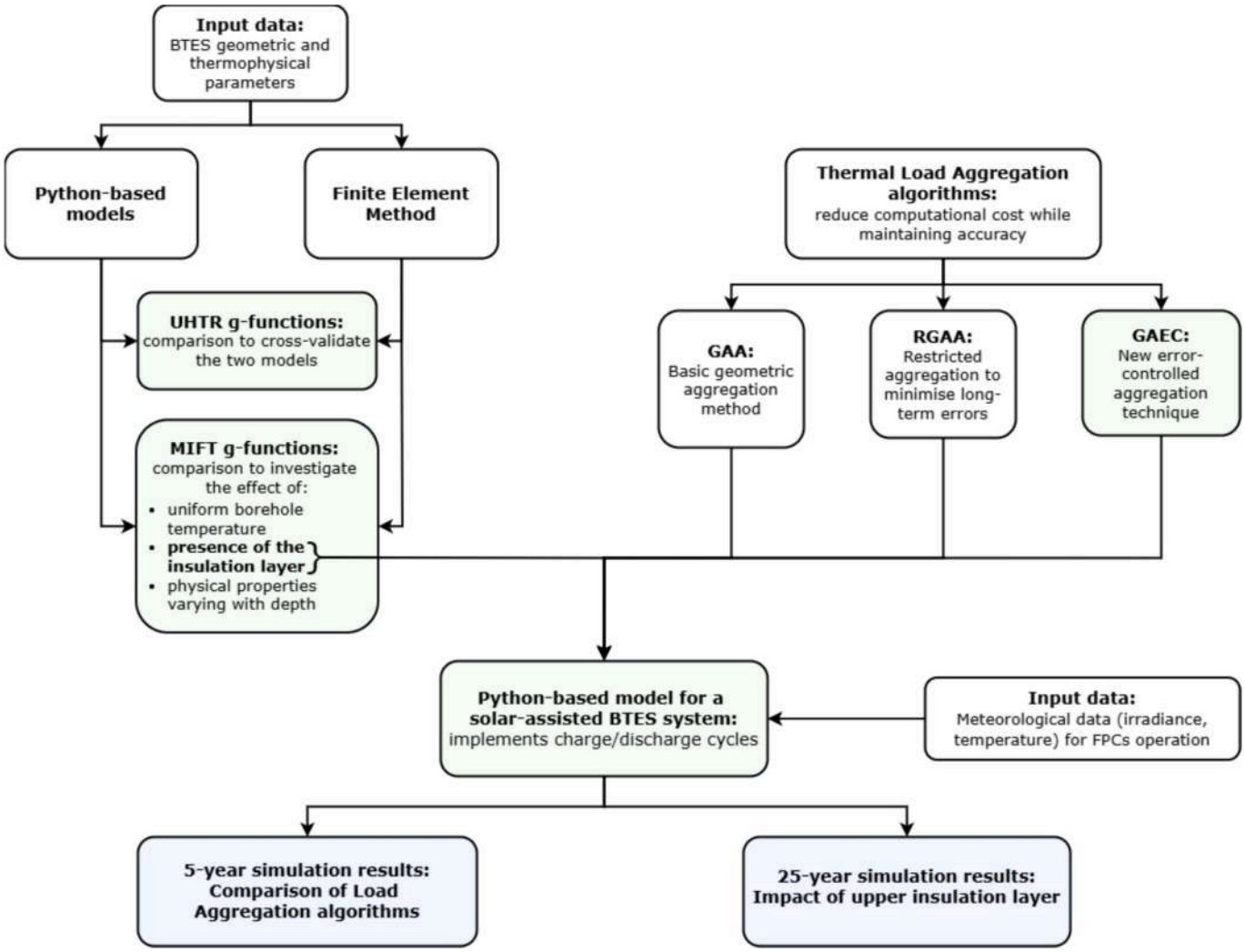

Fig. 2. Methodology block diagram illustrating the different phases of the study. The novel contributions are highlighted in green, and results are shown in blue.

followed by the implementation of thermal load aggregation algorithms (Geometric Aggregation Algorithm, Restricted Geometric Aggregation Algorithm, new Geometric Aggregation with Error Control) to optimize computational efficiency. A Python-based BTES model is finally developed to simulate charge/discharge cycles, incorporating meteorological data as input. Finally, long-term simulations assess load aggregation algorithms performance and the impact of upper insulation. A graphical overview of the methodology is presented in Fig. 2.

3.1. Model of a solar-assisted BTES plant

This section presents the solar-assisted BTES system's modelling framework. It starts with an overview of the layout, followed by the equations for the thermal performance of solar collectors and the BTES. Finally, a detailed explanation of the new aggregation algorithm is provided, outlining its implementation for simulating the system's thermal behavior.

3.1.1. General layout of a solar-assisted BTES plant

A solar-assisted BTES plant is a hybrid energy system that integrates solar energy with underground thermal storage to provide heating and cooling for buildings or industrial processes. The layout of such a plant incorporates solar thermal collectors, which capture solar energy to heat a working fluid, usually water or a water-glycol mixture. Flat-plate solar panels are commonly used, but evacuated tube solar panels or Urban Area Thermal Collectors [36] can also be used depending on the application. The latter represents an innovative approach, as solar energy is absorbed by the road surface. Heat pumps are employed to extract heat from the BTES, thereby enabling the system to provide building space heating during the winter season.

During the charging phase (summer), characterized by high solar availability, heat is collected and transferred via BHEs to the bore field (Fig. 3-a). In this case, the heat transfer fluid flows from the central to the outermost boreholes, whereas the flow reverses during the discharging phase (winter) to extract heat for heating demands (Fig. 3-b). This counterflow arrangement optimizes heat transfer and enables the formation of a radial thermal gradient (thermocline) within the BTES, with higher temperatures at the centre and lower temperatures at the periphery, enhancing storage efficiency and minimizing thermal losses [10].

In this work, a Python model has been developed to simulate the operation of a solar-assisted BTES system. This model represents and simulates the behavior of the two main components of the system. More details regarding the Python code are provided in the attached Supplementary Information.

3.1.2. Flat-Plate collectors model

Flat-plate collectors are the most widely implemented type of solar thermal collector in BTES systems. At Mediterranean latitudes, these collectors achieve suitable temperatures of the heat transfer fluid for the

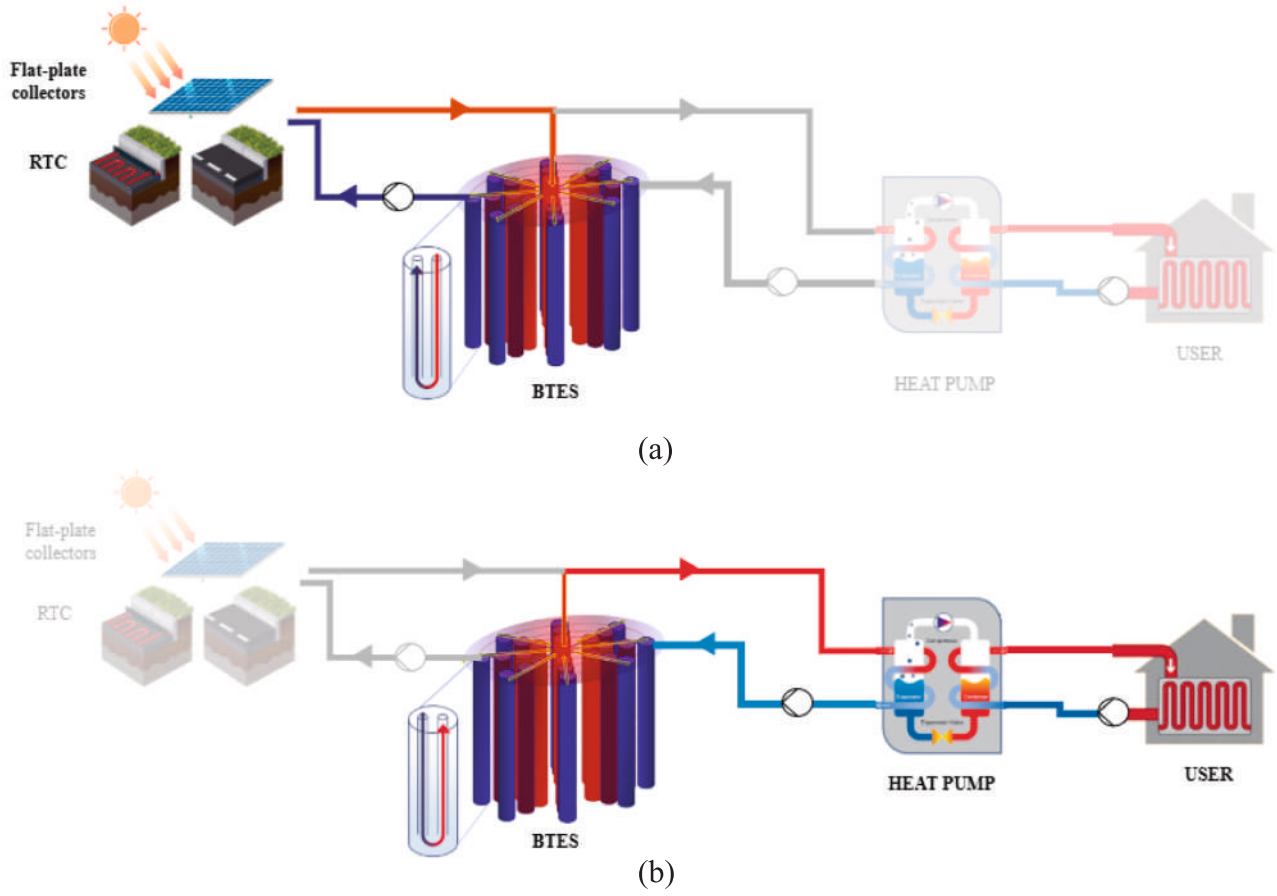

Fig. 3. Operation phases of a solar-assisted BTES: (a) charging and (b) discharging phases. In each phase, inactive system components are shaded to indicate that they are not in use.

charging phase of the BTES, permitting efficient thermal energy storage during periods of high solar irradiation.

The energy balance of the flat-plate collectors is formulated to model the net rate of energy production $\dot{Q}_{sol,net}$ [W] for an array of flat-plate collectors in parallel configuration. The following equations are employed [16]:

$$\begin{cases} \dot{Q}_{sol,net} = n_{FPC} \cdot A_{FPC} \cdot \left[G_{tot} \cdot \eta_0 \cdot IAM - a_1 \cdot (\overline{T}_{FPC} - T_{air}) - a_2 \cdot (\overline{T}_{FPC} - T_{air})^2 \right] \\ \dot{Q}_{sol,net} = n_{FPC} \cdot \dot{m}_{FPC} \cdot c_{pf} \cdot (T_{FPC,out} - T_{FPC,in}) \end{cases} \tag{6}$$

where n_{FPC} is the number of flat-plate collectors, A_{FPC} [m^2] the net collector area, IAM the Incidence Angle Modifier, G_{tot} [W/m^2] the global solar irradiance on the collector plane, η_0 the peak collector efficiency, a_1 [$W/(m^2 \cdot K)$] and a_2 [$W/(m^2 \cdot K^2)$] are two coefficients related to heat loss expression, $\overline{T}_{FPC}$ [°C] is the mean temperature of the fluid in the collector, T_{air} [°C] the ambient air temperature, $T_{FPC,out}$ [°C] and $T_{FPC,in}$[°C] are the outlet and inlet temperatures of the heat transfer fluid in the collector, $\dot{m}_{FPC}$ [kg/s] is the mass flow rate through a single collector, c_{pf} [J/(kg·K)] the specific heat of the working fluid. The IAM provides a correction factor for collector performance by quantifying the reduction in efficiency as the incidence angle θ of the solar beam deviates from perpendicular. It is modelled as follows:

$$\begin{cases} IAM = 1 - b_0 \cdot S - b_1 \cdot S^2 \\ S = \dfrac{1}{\cos(\theta)} - 1 \end{cases} \tag{7}$$

where θ is the incidence angle for beam radiation and b_0 and b_1 are shape parameters specific to the collector.

3.1.3. Energy balance of the BTES

To determine the temporal evolution of the thermal response of both the BHEs and the surrounding soil, heat conservation equations must be solved. These include heat conduction in solid domains (e.g. soil, pipes, grout) and both conduction and convection in the heat transfer fluid domain.

Let V be a volume enclosed by a surface S in the space $\mathbb{R}^3$. For each point P belonging to V, it is possible to write the PDE that models enthalpy conservation as follows:

$$C_p \frac{\partial T}{\partial t} + \overline{\nabla} \cdot \overline{q} = \dot{Q}, \quad \forall P \in V \subset \mathbb{R}^3 \tag{8}$$

where C_p [$J \cdot m^{-3} \cdot K^{-1}$] is the volumetric heat capacity of the soils, T [K] the temperature, t [s] the time, $\overline{q}$ [$W \cdot m^{-2}$] the heat flux density, and $\dot{Q}$ [$W \cdot m^{-3}$] an internal source term.

In most practical BTES systems applications, the following assumptions typically apply:

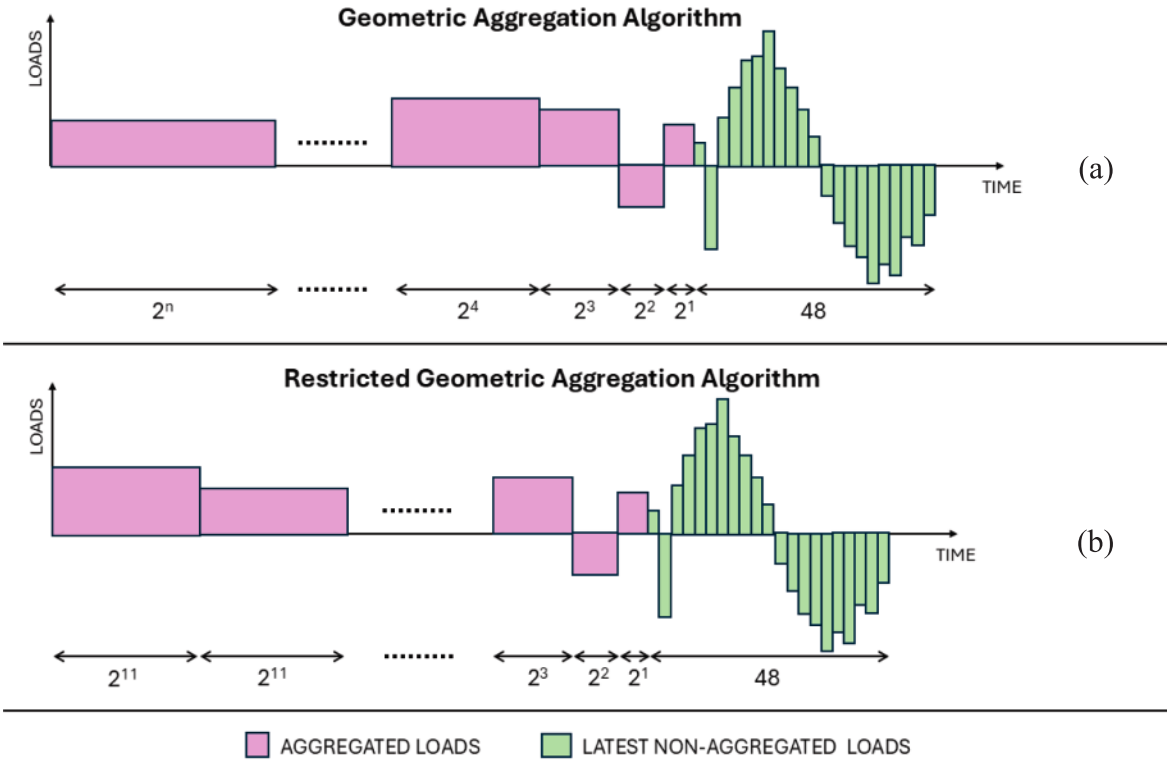

Fig. 4. Graphical representation of: (a) Geometric Aggregation Algorithm, and (b) Restricted Geometric Aggregation Algorithm.

- The boreholes in BTES systems are located in regions where groundwater flow is negligible, resulting in heat transfer predominantly governed by conduction.
- The soils in which the BHEs are constructed can reasonably be assumed to be isotropic with regard to thermal conductivity.

Under these assumptions, the heat flux density $\overline{q}$ can be expressed by the Fourier law as:

$$\overline{q} = -\lambda \cdot \nabla T \tag{9}$$

where λ [W·m^{-1}·K^{-1}] is the thermal conductivity of the solid material (soil, grout or pipes).

The energy balance for the heat transfer fluid can be represented by the following one-dimensional advective-convective PDE:

$$\rho_f \cdot c_{pf} \cdot A_f \cdot \frac{\partial T_f}{\partial t} + \frac{\partial}{\partial x}\left(-\lambda_f \cdot \frac{\partial T_f}{\partial x}\right) \cdot A_f = -\dot{q}_{fs} - \dot{m}_f \cdot c_{pf} \cdot \frac{\partial T_f}{\partial x} \tag{10}$$

where x [m] is the curvilinear abscissa along the development of the pipes, ρ_f [kg·s^{-1}] the fluid density, c_{pf} [J·kg^{-1}·K^{-1}] the specific heat of the fluid, A_f [m^2] the internal cross-sectional area of the pipe, T_f [K] the average temperature of the fluid calculated at x, t [s] the time, λ_f [W·m^{-1}·K^{-1}] the thermal conductivity of the fluid, $\dot{q}_{fs}$ [W·m^{-1}] the thermal power exchanged per unit length of pipe and $\dot{m}_f$ [kg·s^{-1}] the mass flow rate of the fluid.

The coupling term between the two PDEs outlined above is the Equivalent Thermal Resistance R_b [K·m·W^{-1}], which is defined under the assumption of stationary thermal conditions within the borehole as follows [37]:

$$R_b = \frac{\overline{T}_f - \overline{T}_b}{\dot{q}} \tag{11}$$

where $\overline{T}_b$ [K] is the average temperature of the borehole wall and $\dot{q}$ [W·m^{-1}] the heat flux per unit length of borehole. The Equivalent Thermal Resistance R_b can also be expressed as:

$$R_b = \frac{R_f + R_p}{n_p} + R_g \tag{12}$$

where n_p the total number of tubes in each borehole cross section (this number is always twice the number of U-tubes present).R_f is the convective fluid-pipe thermal resistance:

$$R_f = \frac{1}{\pi \cdot D_{p,i} \cdot h_{conv}} \tag{13}$$

where $D_{p,i}$ [m] is the inner diameter of the heat exchanger pipe and h_{conv} [W·m^{-2}·K^{-1}] is the convective heat transfer coefficient. R_p is the conductive thermal resistance of the polyethylene pipe:

$$R_p = \frac{\ln\left(\frac{D_{p,o}}{D_{p,i}}\right)}{2 \cdot \pi \cdot \lambda_p} \tag{14}$$

where $D_{p,o}$ [m] and $D_{p,i}$ [m] are the outer and inner diameter of the pipe, respectively, and λ_p [W·m^{-1}·K^{-1}] the thermal conductivity of the pipe. R_g is the conductive thermal resistance of the grout, which, using a numerical approach by a FE model [38], can be expressed as the ratio of a dimensionless constant C and the thermal conductivity of the grout λ_g [W·m^{-1}·K^{-1}]:

$$R_g = \frac{C}{\lambda_g} \tag{15}$$

The dimensionless constant C depends on the geometry of the borehole (diameter of the borehole, number of pipes, diameter of pipes and their arrangement).

The storage efficiency of BTES systems η_{BTES} is a pivotal performance evaluation metric, which quantifies the ratio between the useful thermal energy retrieved $E_{extracted}$ [MWh] and the total thermal energy injected into the ground $E_{injected}$ [MWh] over the course of a complete storage

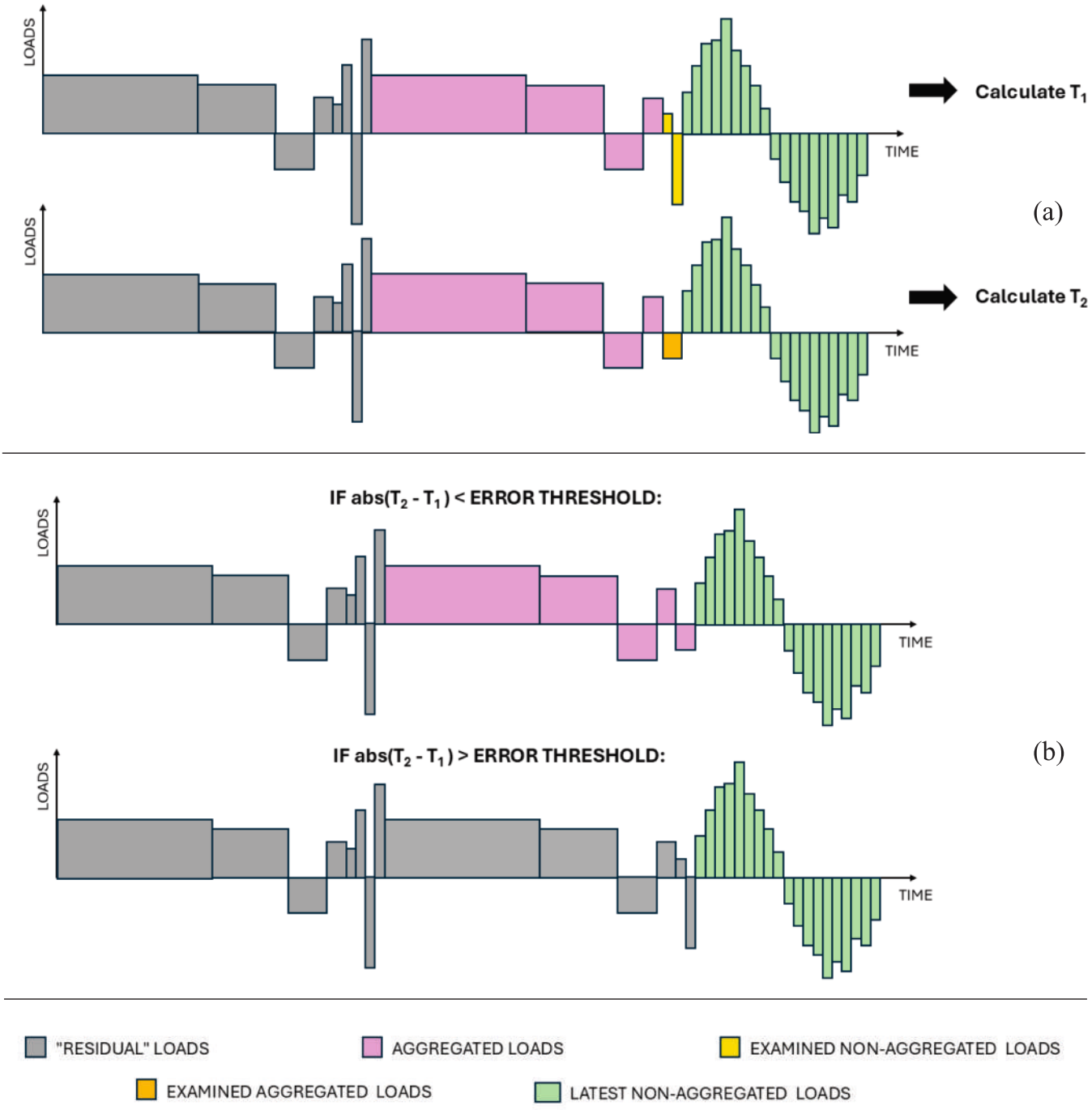

Fig. 5. GAEC algorithm main steps: (a) pre-aggregation and post-aggregation load vectors are used to calculate the average heat transfer fluid temperature, and (b) the load vector is modified after the error checking.

cycle. It allows for the assessment of the overall system performance by accounting for thermal losses to the surrounding soil and is defined as [39]:

$$\eta_{BTES} = \frac{E_{extracted}}{E_{injected}} \tag{16}$$

The total injected $E_{injected}$ and extracted $E_{extracted}$ thermal energies were computed by integrating the thermal power exchanged between the fluid and the BTES over time.

3.1.4. Load aggregation algorithms

The g-function as defined allows for the use of temporal superposition to calculate changes in the bore field, based on a series of thermal loads exchanged between borehole and ground. This is achieved through the implementation of the convolution product [40], as follows:

$$\overline{T}_f(t) = T_0 + \frac{1}{2\cdot\pi\cdot\lambda_s}\cdot\sum_{i=1}^{N}\left[\left(\dot{q}_i - \dot{q}_{i-1}\right)\cdot g\left(\frac{t-t_i}{t_s};\frac{r_b}{H};\frac{B}{H};\frac{D}{H}\right)\right] + R^*_{field}\cdot\dot{q} \tag{17}$$

The main challenge is the indefinite growth of the convolution product terms, therefore requiring the aggregation of past heat loads from previous time periods. Whilst the utilisation of aggregated loads in

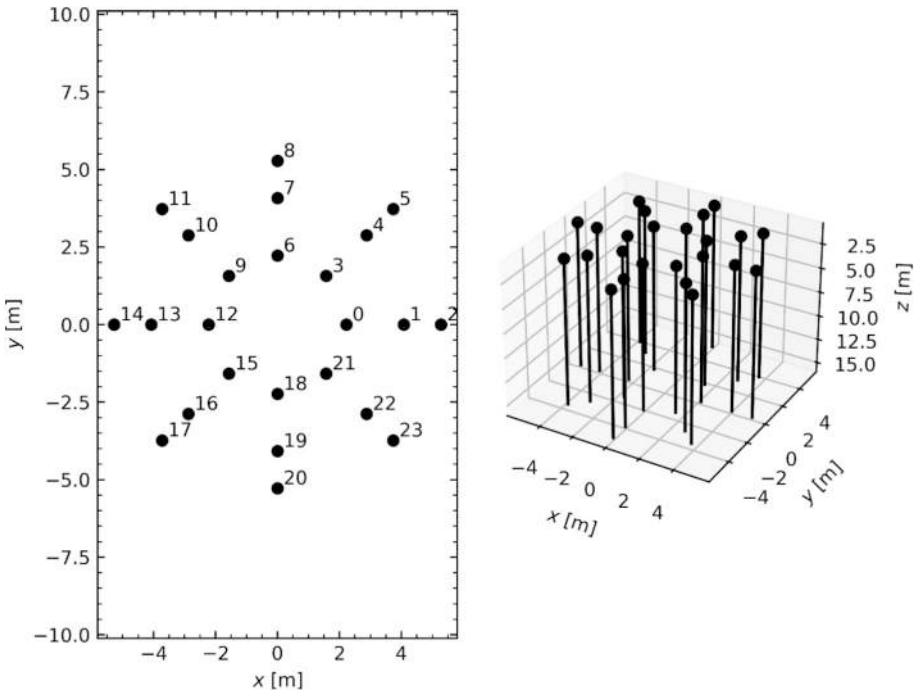

Fig. 6. BHEs layout visualisation in Python.

a subroutine enhances the efficiency of the convolution product calculation, the implementation of an aggregation algorithm introduces an error due to the inevitable loss of information.

In the proposed model, a Geometric Aggregation Algorithm (GAA) was employed at first to manage the updating of aggregated loads [32]. Starting from time t_0, when the fluid temperature is required, and moving in a reverse chronological order, the loads are organised as follows: hours 1–48 remain unaggregated, while hours 49–50 are aggregated together, followed by hours 51–54, 55–62, 63–78, 79–110, and so on, continuing this pattern until the beginning of the time series. Then, an initial modification to the geometric aggregation algorithm was implemented, involving the restriction of the maximum aggregated load size to 2048 h. This modified algorithm is referred to as the Restricted Geometric Aggregation Algorithm (RGAA). A graphical representation of the aforementioned two algorithms is provided in Fig. 4.

Subsequently, a novel algorithm was proposed that accounts for the maximum error introduced by the aggregation process (Fig. 5). At each time step, the new Geometric Aggregation Algorithm with Error Control (GAEC) systematically scans the load vector to identify three loads with the same Δt, in which case it proposes an aggregation based on a geometric series. Both the pre-aggregation and the proposed post-aggregation load vectors are considered to calculate the associated average water temperatures. The absolute error between these temperatures is evaluated, and if it falls below a selected error threshold, the aggregation is accepted, and the loads vector is modified accordingly. Conversely, if the absolute error is greater than the imposed limit, the aggregation current step is not accepted, and the two loads and the loads history prior to them are added to the "residuals" loads, i.e. loads that will no longer be aggregated or scanned by the algorithm. The selection of an appropriate error threshold is pivotal in ensuring that the computational load is not excessively increased.

3.2. Modelling of g-functions for BTES

This section is dedicated to the two methods employed in this study to obtain g-functions. Firstly, the Python *pygfunction* library is utilised, and secondly, the Finite Element Method (FEM) is implemented. Then, the developed FEM models are examined in detail.

3.2.1. The pygfunction library

The *pygfunction* library developed by Cimmino [29] uses analytical methods based on the Finite Line Source (FLS) solution to generate g-functions for borehole fields of arbitrary size and configuration. In the assessment of g-functions, a combination of *pygfunction* modules (boreholes, pipes, networks and media) can be used to define the bore field. Each borehole is then uniformly or non-uniformly discretized in n segments, each representing a finite linear heat source. The g-function module will then be used to evaluate g-functions, by using the most suitable boundary condition.

In particular, using *pygfunction*, two models have been developed to calculate the g-function for a given geometry under both UHTR (Py-UHTR) and MIFT (Py-MIFT) conditions. These models allow for the evaluation of the impact of different boundary conditions on the thermal response of the bore field. The Python code used to obtain the g-functions under both UHTR and MIFT conditions is provided in the Supplementary Information.

The *pygfunction* library also facilitates the visualisation of the BHEs layout, as illustrated in Fig. 6 for the case study of this paper that will be later discussed.

3.2.2. Finite Element model of the BTES

In addition to the analytical and semi-analytical tools like *pygfunction* for evaluating the thermal response of a BTES system, FE modelling provides a powerful alternative for extracting the g-function and analysing the system's thermal performance. FE models enable a more comprehensive representation of the physical processes by solving the governing PDEs in three-dimensional geometries capturing complex effects, such as the thermal interaction between boreholes and heterogeneous subsurface properties. More details on the techniques used for modelling the complex boundary conditions of the FEM models are described in the attached Supplementary Information.

Given the axisymmetric borehole configuration of the BTES, a reduced model is proposed. In the case study's eight-member array, the model represents half of a single sector (Fig. 7-a). This approach takes full advantage of the inherent symmetry conditions of the BTES, significantly reducing computational complexity while preserving accuracy. The average thermophysical properties of the soil are selected as

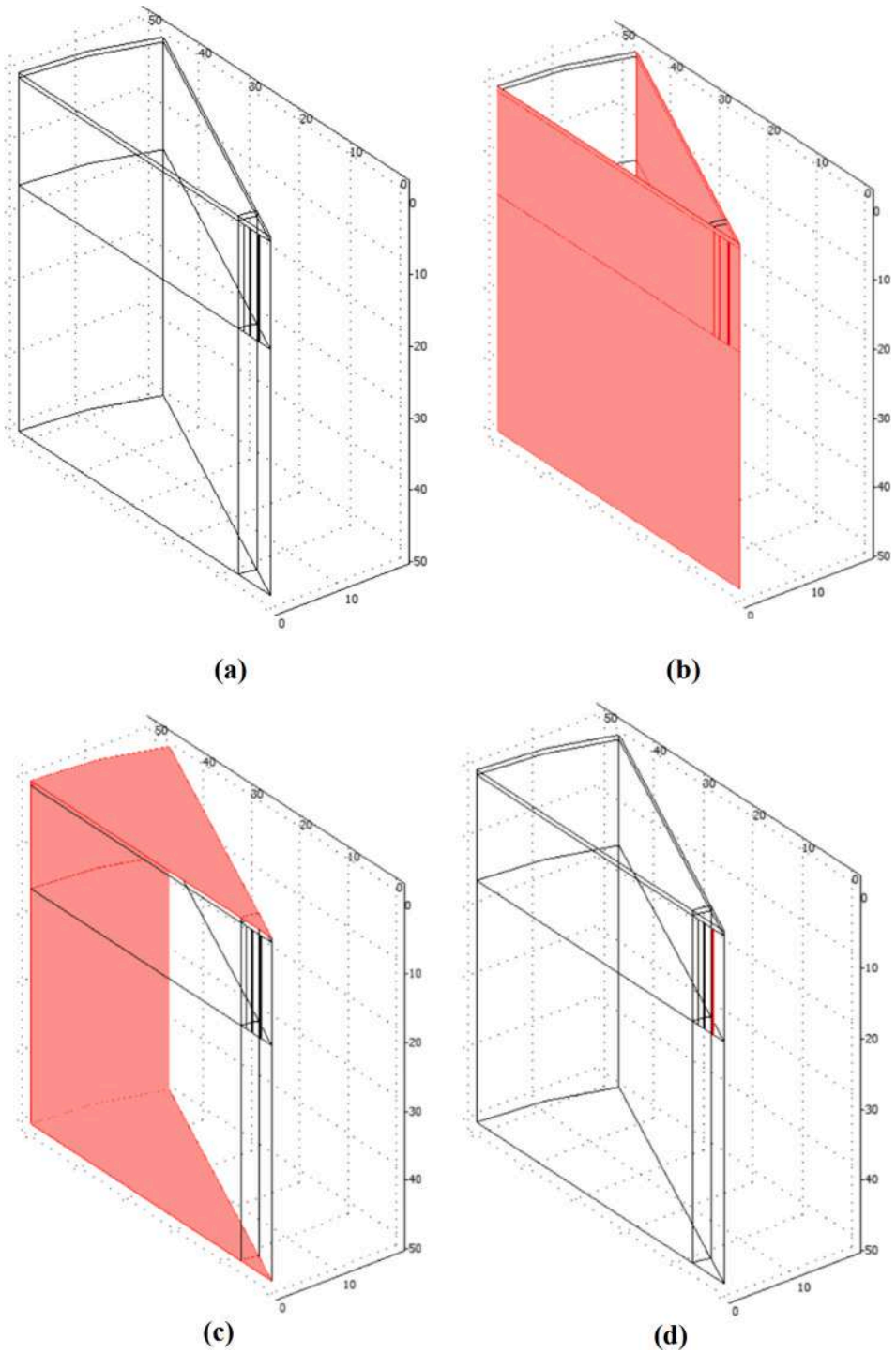

Fig. 7. Three-dimensional FE UHTR model of the BTES: (a) 3D semi-sector, (b) adiabatic boundaries, (c) constant temperature boundaries, and (d) heat flux boundaries.

model parameters, with an undisturbed soil temperature profile set as the initial condition of the problem. In the present work, six FE models of increasing complexity are proposed to estimate g-functions (FE UHTR A S1, FE MIFT 1-A S1, FE MIFT 2-A S1, FE MIFT 2-A S2, FE MIFT 2-B S1, FE MIFT 2-C S1). All these models share the same boundary condition for the planes of geometric and thermal symmetry (Fig. 7-b), where a Neumann condition with zero heat flux is imposed. Also referring to Table 1, the differences among the models are as follows:

- In the FE UHTR A S1 a uniform and constant heat flux is imposed in all the borehole walls (Fig. 7-d). Moreover, the model does not include the grout volume, but the coupling with Eq. (10) is achieved using R_b. In addition, a Dirichlet boundary condition with a uniform and constant value of the soil temperature, equal to T_0, is imposed both on all other boundaries (Fig. 7-c). Finally, this model does not consider the presence of an insulation layer at the top surface (condition named A) and the initial condition and physical properties of the different materials are assumed constant in time and space according to a scenario which is named S1. The FE UHTR model is

Table 1
Overview of the developed FE models.

	Symmetry planes	Borehole walls	Pipe walls	Upper surface (*)
FE UHTR	Adiabatic condition	$\dot{q} = const.$	–	A
FE MIFT 1	Adiabatic condition	Mixed condition	–	A
FE MIFT 2	Adiabatic condition	–	Mixed condition	A, B, C

(*) The developed models can include three different types of boundary conditions at the upper surface: (A) a non-insulated BTES, where the top layer consists of soil; (B) a BTES with an insulating layer; and (C) a BTES with an adiabatic upper boundary.

primarily employed to test the adequacy of the domain size and mesh resolution, rather than to represent realistic BTES configurations. Since it assumes a uniform heat flux distribution, it is not suitable for simulating systems with boreholes connected in series.

- The FE MIFT 1-A S1 does not explicitly consider the volume of pipe, grout and fluid, as the FE UHTR A S1, but considers boreholes connected in series by imposing that the outlet temperature of one BHE is the inlet temperature of the next, and a coupling with Eq. (10) through mixed boundary conditions applied at the borehole wall, which are described below. A schematic representation of the mixed boundary condition implementation for MIFT 1-A S1 is shown in Fig. 8-a. In FE MIFT 1-A S1, the 3D FE model is coupled with a 1D FE model which simulates the fluid flow through three BHEs connected in series via three advective-convective PDEs (one for each borehole).
- The four remaining models of the FE MIFT 2 type consider boreholes connected in series as in the previous model. However, they differ from the previous model in that they take into account the grout volume in the 3D FE model and all descending and ascending branches of the three BHEs (resulting in six PDEs). For all models FE MIFT 2 (Fig. 8-b), the conditions imposed on the outer walls of the tube of the U-exchangers are mixed (see below). The FE MIFT 2 models are differentiated by applying three different conditions to the upper boundary of the BTES: uninsulated (condition A), insulated with an insulating layer (condition B), and adiabatic (condition C). Finally, only for FE MIFT 2-A, in addition to the S1 scenario, a S2 scenario was considered in which both the thermal profile and the physical properties of the soils are variable with depth.

The more advanced FE MIFT models are used to assess the physical adequacy of the *pygfunction* MIFT boundary conditions in capturing the actual heat exchange processes within the BTES. The differences observed between FE MIFT simulations and simplified assumptions help quantify the impact of boundary condition choices on the system's thermal response.

As already stated above, in FE MIFT models the coupling of the 3D solid (Eq. (8) and the 1D fluid (Eq. (10) domains, represented by Eq. (11), is achieved by imposing a mixed boundary condition.

In FE MIFT 1, the basic 3D FE model outlined above is coupled with a 1D FE model that simulates the fluid flow through three BHEs connected in series via three advective-convective PDEs (one for each borehole). The 1D fluid domain is modelled as a single branch with an equivalent double cross-sectional area to account for both flow directions, without distinguishing between downstream and upstream flow. The series connection is ensured by imposing that the outlet temperature of one BHE is the inlet temperature of the next. To couple the 1D fluid and 3D solid domains, the mixed boundary condition is imposed at the borehole walls. Specifically, this portion of the boundary (namely, the borehole walls) requires the imposition of a Neumann heat flux condition $\dot{q}_N$, whose value depends on two other variables: the borehole wall temperature T_b (from the 3D domain) and the fluid temperature T_f (from the 1D domain). The existing system already includes two governing equations, but a third equation must be introduced through the coupling of the two domains to determine the heat flux $\dot{q}_N$. The implementation of this complex mixed boundary condition in the Multiphysics models is described in detail in the Supplementary Information.

In FE MIFT 2, the same procedure is applied at the individual pipe level within the BHEs. The two unknowns in this case are the pipe wall temperature T_p (from the 3D domain) and the fluid temperature T_f (from the 1D domain). This approach leads to six PDEs, each corresponding to the ascending and descending branches of the three BHEs in series. Unlike the previous model, this time the actual pipe geometry is considered, meaning that the cross-sectional area used in the governing equations corresponds to the real pipe dimensions. Only for FE MIFT 2 models the heat flux exchanged between the fluid and the solid domains is calculated by considering a thermal resistance equal to $(R_f + R_p)$. Indeed, in FE MIFT 2 the grout is included in the 3D solid domain and its thermal behavior is consequently directly captured, allowing for a more accurate representation of the short-term time response of the system.

A graphical representation of the procedure for the implementation of the mixed boundary condition for FE MIFT 1 and FE MIFT 2 models is shown in Fig. 8.

For all models, selecting appropriate domain dimensions is crucial to ensuring that the numerical solution is not influenced by boundary conditions. To this end, the domain size must be incrementally increased until further enlargement ceases to impact the numerical results. This process also allows for cross-validation, as will be described below.

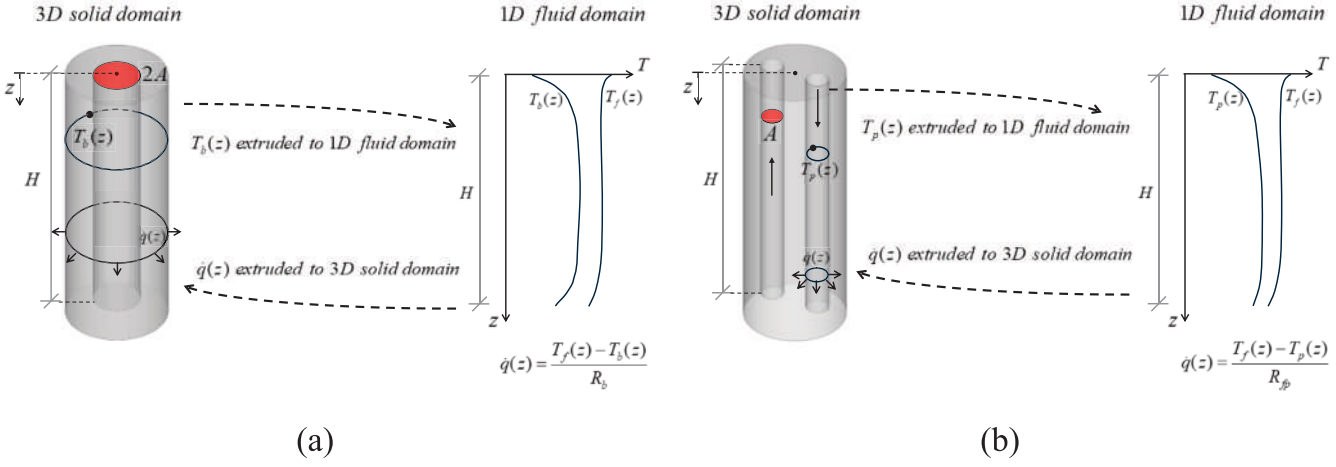

Fig. 8. Schematic representation of the mixed boundary condition implementation for: (a) FE MIFT 1, and (b) FE MIFT 2.

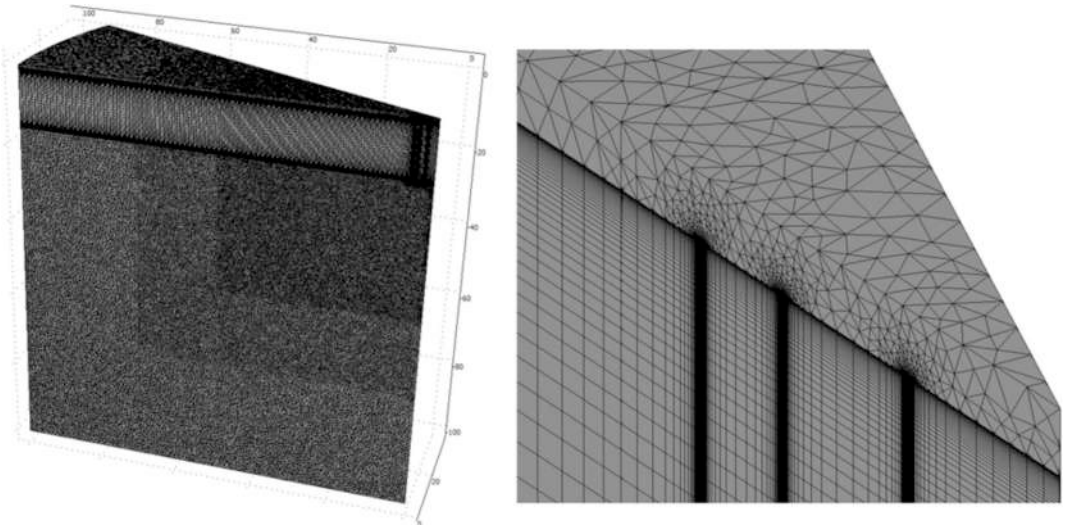

Fig. 9. Mesh used to spatially discretize the BTES domain.

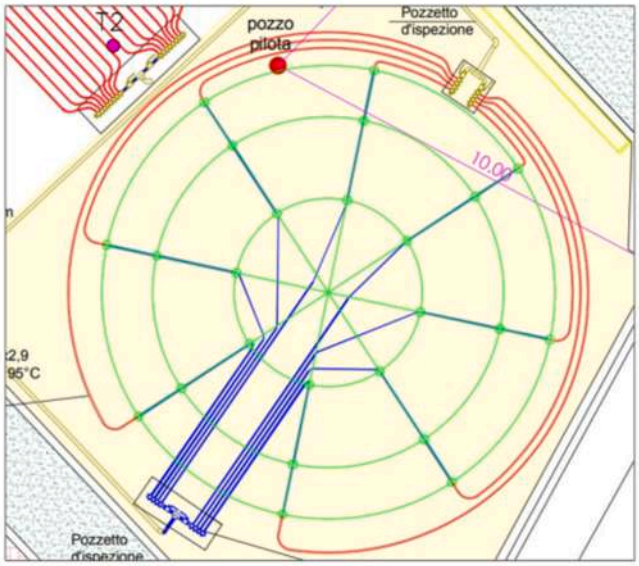

Fig. 10. BTES layout with arrangement of the 24 BHEs and related hydraulic connections. The heat exchangers are arranged in U–tubes and interconnected in parallel-series circuits. An insulation layer covers the superficial bore field area, encompassing the area outlined by the yellow polygon.

Particular attention must also be given to the three-dimensional mesh used to discretize the calculation domain. Since the number of mesh linear elements depends on the domain size, it is essential to refine the discretization to achieve a better solution accuracy while maintaining computational efficiency. Consequently, the mesh density is increased near the borehole walls of the BTES, as shown in Fig. 9, where the highest thermal gradients are expected.

4. Case study and numerical analysis

4.1. Schematic description of the studied plant

In order to validate the proposed modelling approach and to study the performance of a real solar-assisted BTES system, the coupling of an existing BTES system with a solar thermal field is analysed. The BTES under investigation is the one installed in a car park on the University of Palermo campus as part of the SMARTEP project [31] and is one of the few BTES systems present in the Mediterranean (see Fig. 10). The 24 BHEs are arranged in an axisymmetric layout along three concentric circumferences with radii of 2.23 m, 4.07 m, and 5.28 m radii, defining a conventional bore field radius of 6.43 m (defined according to the Hellstrom's DST model [24]). An insulation layer with thermal conductivity reported in Table 3 is placed above the entire superficial bore field area, as shown in Fig. 10. The BHEs layout and connections during the construction stage are shown in Fig. 11.

The heat exchangers are U-shaped PeX-A tubes. The BHEs located on the innermost circumference are connected to each other in parallel, and

Fig. 11. Installation phase of the SMARTEP BTES System at the University of Palermo.

Table 2
Geometric parameters of the BHEs considered in the FE models and in the Python model.

Parameter	Value
pipe outer diameter [m]	0.032
pipe inner diameter [m]	0.026
half of the shank space [m]	0.039
BHE diameter [m]	0.140
BHE depth [m]	15
burying depth [m]	0.70

Table 3
Models subdomains' thermophysical properties.

Sub-domain	Parameter	Units	Value
Heat Transfer Fluid	density,ρ_f	[kg/m^3]	1000
Heat Transfer Fluid	thermal conductivity,λ_f	[W/(m·K)]	0.60
Heat Transfer Fluid	specific heat,c_{pf}	[J/(kg·K)]	4200
Pipe	density,ρ_p	[kg/m^3]	932
Pipe	thermal conductivity,λ_p	[W/(m·K)]	0.42
Pipe	specific heat,c_{pp}	[J/(kg·K)]	2300
Grout	thermal conductivity,λ_g	[W/(m·K)]	1.475
Grout	volumetric heat capacity,C_g	[J/(m^3·K)]	$3.9{\cdot}10^6$
Soil	thermal conductivity,λ_s	[W/(m·K)]	1.68
Soil	volumetric heat capacity,C_s	[J/(m^3·K)]	$2.351{\cdot}10^6$
Insulating layer	thermal conductivity,λ_{ins}	[W/(m·K)]	1.42

each of these exchangers is connected in series to another exchanger located on the next outer circumference. Finally, all heat exchangers on the outermost circumference are connected to each other in parallel. The geometric parameters describing the BHEs are summarized in Table 2.

4.2. Calibration of the numerical models

Numerical and in-situ experimental investigations were previously conducted using a pilot BHE and Thermal Response Tests to characterise the thermophysical properties of soils and materials [36]. As a result of these investigations, the profile of the thermal conductivity of the soil with depth was revealed. Furthermore, the measurements determined an undisturbed average soil temperature T_0 of 20 °C. The thermophysical properties of the subdomains in the models are shown in Table 3.

In Scenario 1, the material properties are always assumed to be constant and homogeneous throughout the domain, whereas in Scenario 2 the volumetric heat capacity through the domain varies as follows:

$$C_{soil} = \begin{cases} C_s & for\, z > -35 \\ C_{clay} & for\, z \le -35 \end{cases} \tag{18}$$

where C_{clay} is the volumetric heat capacity of clay and is equal to $2.83{\cdot}10^6$ [J/(m^3·K)]. The variation in thermal conductivity is described as:

$$\lambda_{soil} = \begin{cases} \lambda_s & for\, z > -35 \\ \lambda_{clay} & for\, z \le -35 \end{cases} \tag{19}$$

where λ_{clay} is the thermal conductivity of clay and is equal to 1.76 [W/(m·K)]. Finally, the initial temperature profile through the domain varies as follows:

$$T_{soil} = \begin{cases} T_0 & for\, z > -35 \\ T_0 - \dfrac{\overline{q}_h}{\lambda_{clay}} & for\, z \le -35 \end{cases} \tag{20}$$

where $\overline{q}_h$ is the endogenous heat flux for continental area [41], that in the present study is assumed to be equal to 0.0709 [W/m^2].

For SMARTEP's BTES system, the following equivalent thermal resistances were used in the developed models:

- Convective fluid-pipe thermal resistance $R_f = 0.0070$ [m·K/W]: calculated using Equation (13) for a reference flow rate of 0.1814 kg/s per U-tube, which approximately represents the overall flow conditions during the charging phase. The convective heat transfer coefficient was computed using *pygfunction* based on the following thermophysical properties of water at 20 °C: specific heat $c_{p,f} = 4200$ [J/kg·K], density $\rho_f = 1000$ [kg/m^3], dynamic viscosity $\mu_f = 8.88{\cdot}10^{-4}$ [kg/m], thermal conductivity $\lambda_f = 0.607$[W/m·K]. The resulting convective heat transfer coefficient was approximately $h_{conv} = 1746.28$ W/m^2·K.

Table 4
Operating data ARCON Solar, HT-A 35–10.

Parameter	Value
A_{FPC} [m^2]	20
η_0 [-]	0.845
a_1 [W/(m^2·K)]	2.94
a_2 [W/(m^2·K^2)]	0.013
b_0 [-]	0.1316
b_1 [-]	−0.005

Table 5
Meteorological data for Palermo: monthly average, minimum, and maximum air temperatures (T_{air}),and monthly radiation on the plane of array (H_{POA}).

	T_{air} [°C]			H_{POA} [kWh/m^2]
	min	**max**	**average**	
January	5.75	19.30	12.30	87.20
February	5.10	21.00	12.20	108.00
March	6.70	23.70	13.90	157.00
April	10.20	25.95	15.90	170.00
May	13.30	29.50	19.30	194.00
June	16.20	32.05	22.90	190.00
July	20.50	37.50	26.40	202.00
August	20.80	35.10	26.80	198.00
September	17.65	33.85	23.80	160.00
October	14.20	30.30	20.90	139.00
November	10.45	28.60	17.10	97.30
December	7.70	22.25	14.10	80.70

- Conductive thermal resistance of the polyethylene pipe $R_p = 0.0787$ [m·K/W]: estimated using Equation (14), based on the pipe diameters reported in Table 2.
- Conductive thermal resistance of the grout $R_g = 0.074$ [m·K/W] and dimensionless constant $C = 0.10$: obtained from a previous study [31] for the same BTES system using FE modeling and the Flow Net Method [38]. For validation purposes, a comparison was made with the multipole method for single U-tube borehole heat exchangers [42], using a first-order approximation. The resulting resistance $R^1_{g,multipole} = 0.0731$ [m·K/W] closely matches the value obtained with the Flow Net Method ($R_g = 0.074$[m·K/W]), thus confirming the reliability of the adopted value.
- Equivalent thermal resistance $R_b = 0.1163$ [m·K/W]: calculated as in Equation (12).
- Effective thermal resistance $R^*_{field} = 0.1187$ [m·K/W]: calculated according to Equation (4).

The charging of the BTES is achieved through the integration of a 20 m^2 solar thermal field, with the Flat-Plate Collectors characterized by the parameters delineated in Table 4. The surface area was selected to achieve a maximum temperature at the start of the discharge period that is suitable for integration with heat pumps [16].

The charging phase, which occurs from April to October, is characterized by a flow rate of 11 m^3/h to ensure the presence of turbulence (Re = 20000) within the BTES tubes. The BTES discharging phase spans from November to March and is subject to a flow rate of 2.5 m^3/h to maintain minimal turbulence inside the tubes of the BTES (Re = 2300). In the discharging phase, it is assumed that the heating system will be operational from 8 a.m. to 7p.m., requiring a constant load from the BTES. This constant load was selected so that, during the discharging period, about 70 % of the energy transferred to the BTES during the charging phase could be extracted.

4.3. Climatic conditions of the case study site

The case study site is located in Palermo, Italy, a city situated on the northern coast of Sicily and characterized by a Mediterranean climate

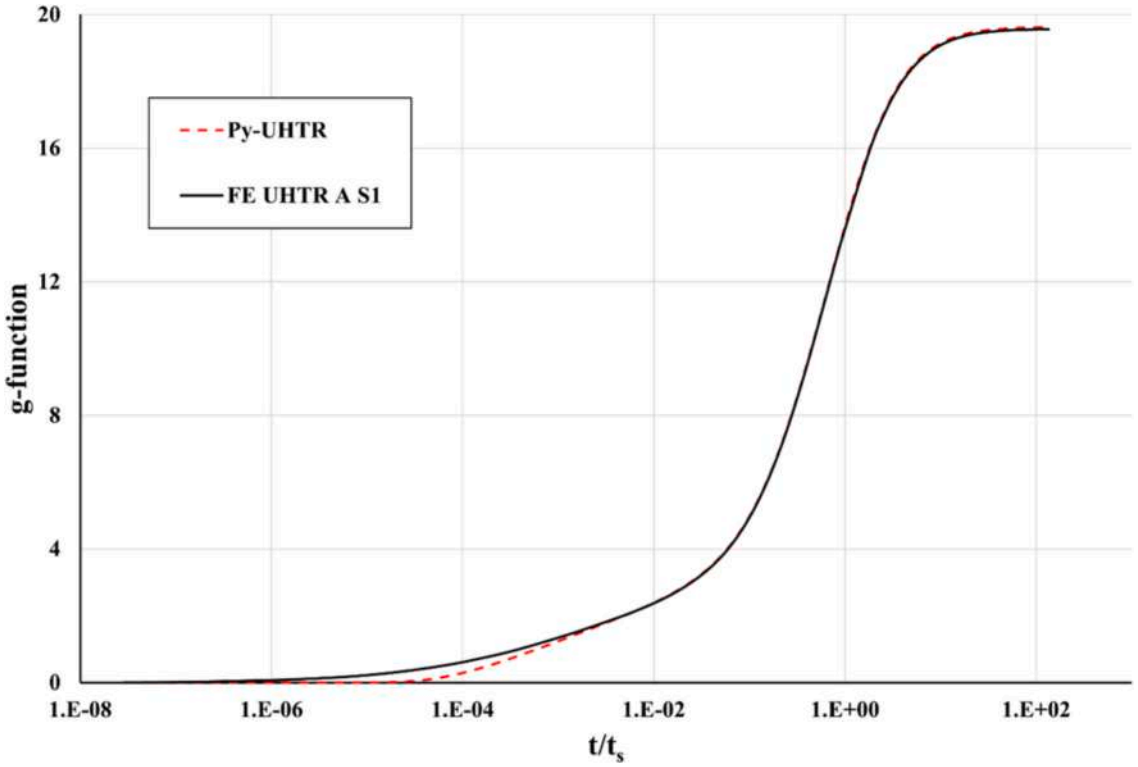

Fig. 12. Comparison of g-functions for the UHTR case obtained with COMSOL and *pygfunction*.

[43], featuring mild and relatively wet winters and hot, dry summers. During the winter months, average temperatures generally range between 8 °C and 14 °C, while in summer they typically span from 21 °C to 28 °C, with extreme values occasionally exceeding 35–40 °C and an annual cumulative radiation reaching about 1800 kWh/m^2. To provide context for the simulations, Table 5 reports the monthly average, minimum, and maximum air temperatures T_{air}, and the monthly radiation on the plane of array H_{POA} for Palermo. The meteorological data for Palermo used for the simulations is provided in Supplementary Information.

4.4. Comparison analysis among the different studied g-functions

In order to model the g-function under UHTR and MIFT conditions, transient numerical simulations were conducted, assuming a constant total heat flux exchanged for a time corresponding to 150 years, for which it can be assumed that steady-state thermal conditions are reached throughout the calculation domain. Under UHTR conditions, a constant heat flux per unit length equal to 22.2 W/m is imposed on the borehole in COMSOL Multiphysics®, whilst under MIFT conditions, a constant thermal jump (the temperature difference between the inlet of the first BHE and the outlet of the last BHE in the series) equal to 0.4°C is imposed. Then, in the post-processing phase, the temporal variation of the mean temperature of the borehole walls is calculated. Eq. (1) is finally utilized to derive the g-function. A detailed description of all the steps involved in the creation of a FEM model can be found in the Supplementary Information.

4.4.1. Cross-validation of the FEM and Python models using UHTR conditions

Given that the UHTR conditions are the simplest to model in FEM, a comparison was made between the Py-UHTR and FE UHTR-A S1 models to cross-validate the solutions. In other words, the solution obtained with Python was regarded as an analytical reference solution with which to compare the numerical solution obtained with COMSOL. Iterative modification of the domain width and mesh definition was then employed until the g-functions generated by both models were as close as possible. This proposed procedure emphasizes the importance of employing different numerical methodologies to define models that are both accurate and reliable.

4.4.2. G-functions generation under different boundary conditions

The second set of analyses was carried out on the other five FE MIFT models and the Py MIFT model in order to validate the different physical and simplifying assumptions underlying each of these models. The g-functions generated by the following models were compared:

- Py MIFT, FE MIFT 1-A S1, FE MIFT 2-A S1, in order to evaluate the different simplifying assumptions with which the borehole is modelled.
- FE MIFT 2-A S1, FE MIFT 2-B S1, FE MIFT 2-C S1 for testing different isolation conditions at the upper boundary.
- FE MIFT 2-A S1, FE MIFT 2-A S2 to evaluate the effect of different initial conditions and material properties.

4.5. Energy analysis of the investigated system

The Python model that implements the layout of the case study was used to conduct dynamic simulations of the system's charge and discharge cycles. These simulations were based on hourly irradiance data from a Typical Meteorological Year for the location of Palermo, Italy, provided in Supplementary Information. The analyses were aimed at both testing the accuracy of the aggregation algorithms and evaluating the effect of top isolation on the dynamic response of the Solar Assisted BTES system. The following simulations were carried out:

- First analysis – Simulation of the first 5 years of operation, using the FE MIFT 2-A S1 curve and testing three different aggregation algorithms: GAA, RGAA and GAEC. The GAEC algorithm was also analyzed with two different tolerances: 0.1 °C (GAEC-0.1) and

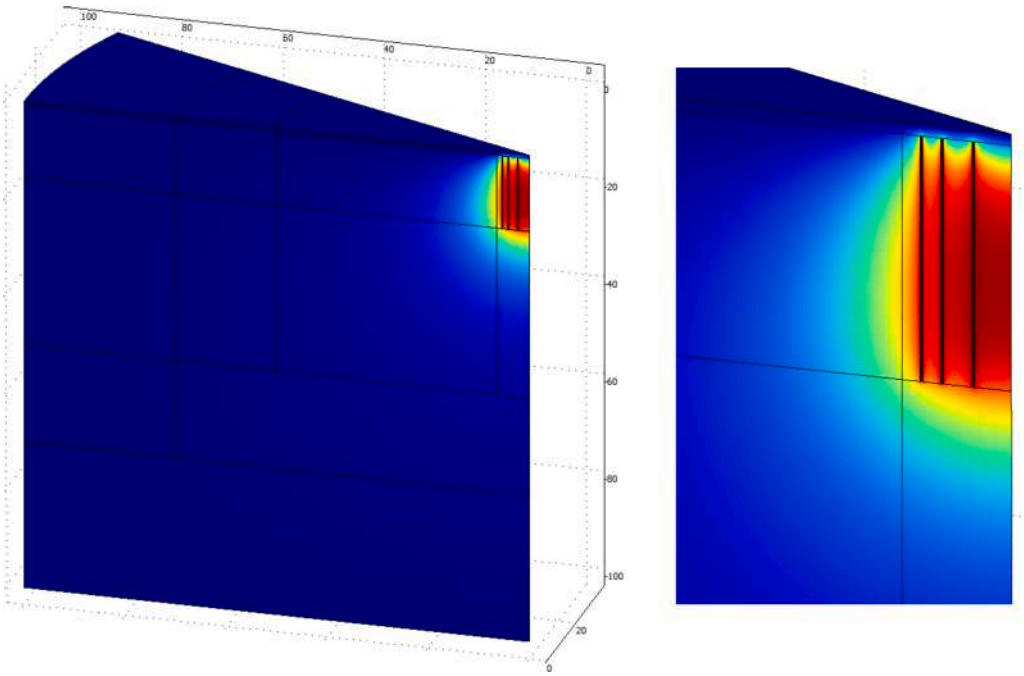

Fig. 13. Contour plot of the BTES temperature (COMSOL 150 years simulation for the UHTR case).

0.05 °C (GAEC-0.05). Finally, the simulation of the first 5 years of operation without any aggregation of loads was carried out.

- Second analysis – Simulation of the first 25 years of operation, comparing the results obtained with the g-functions FE MIFT 2-A S1 and FE MIFT 2-B S1, using the new algorithm.

All simulations were performed on a workstation equipped with an Intel® Core™ i7-10700 CPU @ 2.90 GHz (8 cores, 16 logical processors), 32 GB RAM, and running Windows 10 Pro. The system includes both an integrated Intel® UHD Graphics 630 and a dedicated NVIDIA® GeForce RTX 3060 Ti GPU.

The evaluation of the accuracy of the simulations was conducted by calculating both the Absolute Error (AE) and the Mean Absolute Error (MAE). Absolute Error is a measure of the difference between a reference value and a predicted value, expressed as a non-negative number, and can be expressed as follows [44]:

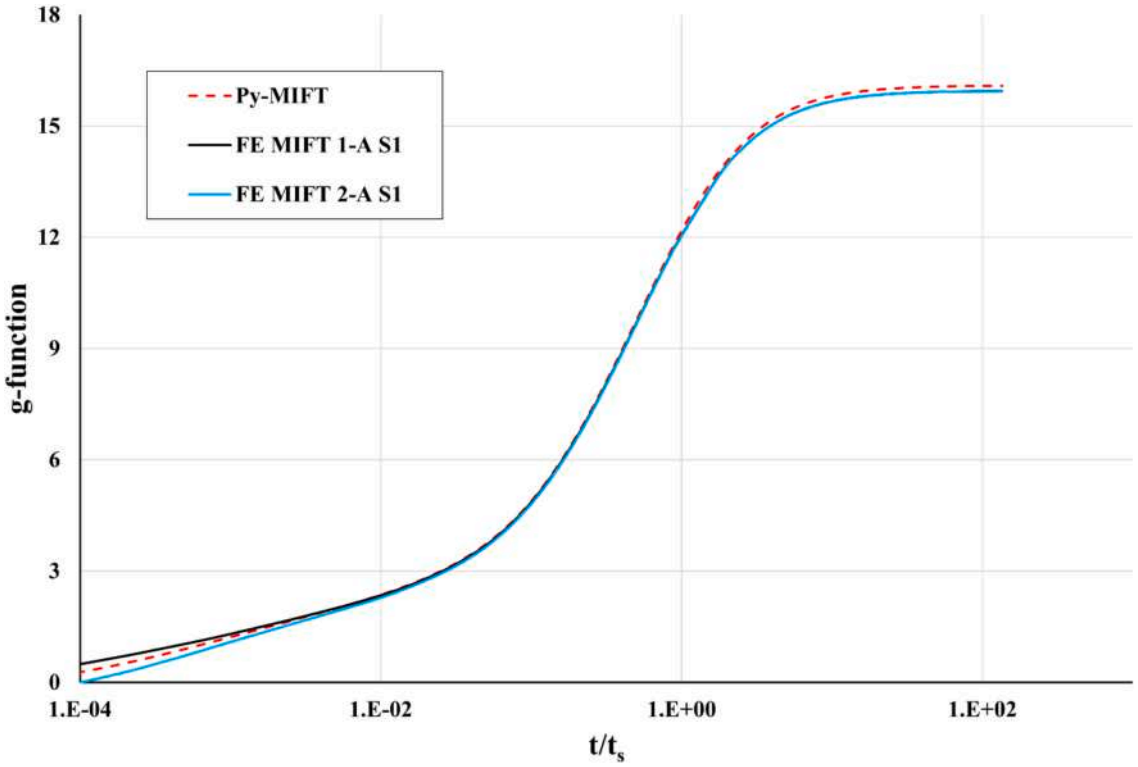

Fig. 14. Comparison of g-functions for the MIFT case obtained with COMSOL and *pygfunction*.

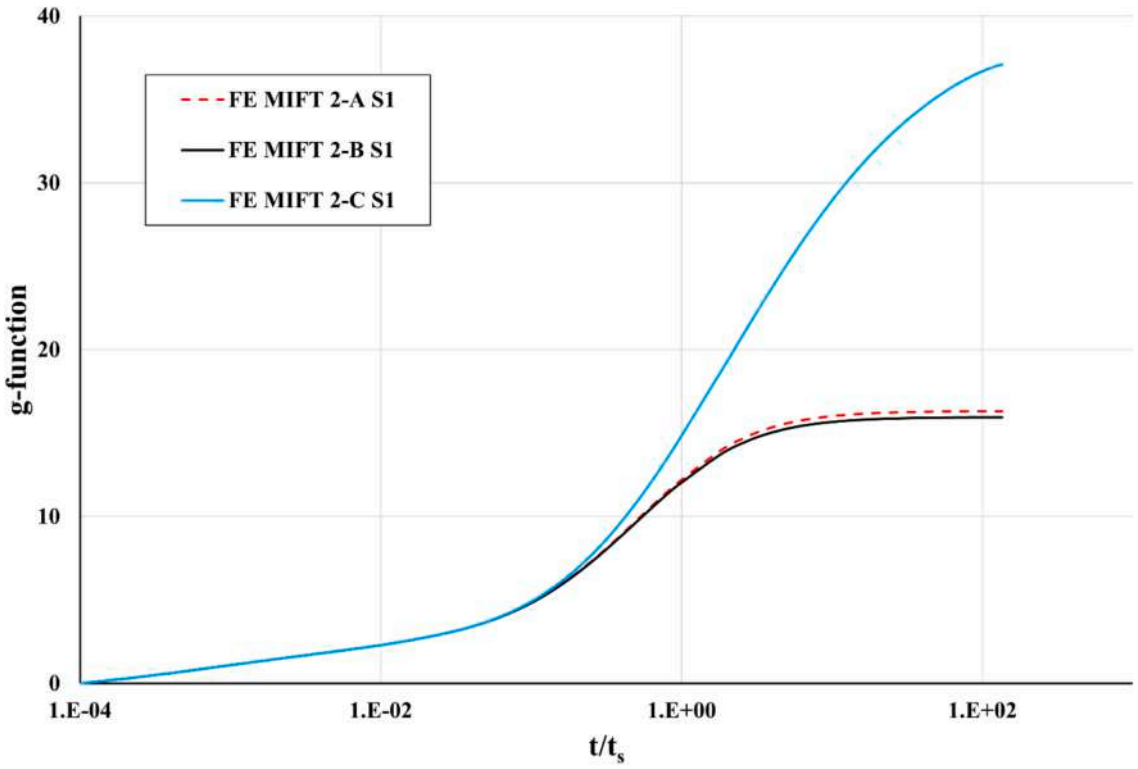

Fig. 15. Comparison of g-functions for the MIFT case obtained with COMSOL to investigate the impact of the upper boundary insulation layer of the BTES.

$$AE = \left|\overline{T}_{w,ref} - \overline{T}_{w}\right| \tag{21}$$

where $\overline{T}_{w,ref}$ and $\overline{T}_{w}$ are the reference value and the predicted value of the hourly average heat transfer fluid temperature, obtained respectively without a load aggregation algorithm and with the tested load aggregation algorithm.

MAE represents the average of the absolute differences between the reference values and the values predicted by the model, without considering the sign of the error, and can be calculated as follows [45]:

$$MAE = \frac{1}{N}\sum_{i=0}^{N}\left|\overline{T}_{w,ref} - \overline{T}_{w}\right| \tag{22}$$

where N is the total number of hourly temperature values obtained from the simulation.

The calculation of both AE and MAE is required to better understand the models' accuracy. The Absolute Error represents the deviation between the reference and predicted values for a single data point, providing a measure of the maximum error within a specific simulation period. It is particularly useful for identifying the largest errors that occur during the simulation. On the other hand, the Mean Absolute Error (MAE) is the average of the absolute errors across all time steps in the simulation, giving a more comprehensive view of the overall accuracy of the algorithm by providing a measure of how well the model performs on average over the entire simulation period. This facilitates a more thorough evaluation of the model's accuracy and enables the identification of any systematic biases or trends in the predictions.

5. Results and Discussion

5.1. Validation of the numerical model

Fig. 12 gives a comparison between the g-functions obtained from the FE UHTR A S1 and the Py-UHTR. After 150 years, when the stationary condition is reached, the maximum value of the g-function is 19.56. It can be seen from the results of these simulations that the curves obtained for the SMARTEP BTES are practically superimposable when the domain for the FEM simulations is characterised by a radius 20 times that of the BTES (i.e., the radius of the circular area containing all boreholes) under examination. The number of mesh elements for the chosen volume domain is approximately 7 million (7102471 mesh elements), with more than 2 million degrees of freedom (2028059 degrees of freedom). However, the UHTR condition, while advantageous for numerical comparisons between models due to its ease of implementation, remains unrealistic for simulating the operation of BTES systems. These g-functions are rather more suitable for simulating the operation of GSHP systems, whose BHEs are much longer and are mostly hydraulically fed in parallel.

In Fig. 13, the temperature contours in the BTES obtained from the FE UHTR A S1 after 150 years are displayed. This figure illustrates the volumes of soil most impacted by heat exchange, showcasing in the detail the significant cooling effect of the upper part of the BTES due to heat loss to the external environment.

The two solutions have been shown to be in agreement in terms of the g-function. Despite the higher complexity and computational load, it is only through the implementation of the FE model that the areas of the soil volume that heat up and cool down can be identified through thermal field analysis.

5.2. Comparison of the analysed g-functions

The following Fig. 14 illustrates the g-functions under the MIFT assumptions corresponding to three of the developed models, i.e. Py MIFT, FE MIFT 1-A S1, and FE MIFT 2-A S1. These functions are more suitable for the modelling of the typical series and parallel connections observed in BTES systems. Compared to the previous case (19.56 after 150 years), they have a lower long-term maximum value (about 16 after 150 years). The first implication is that neglecting connections in a BTES can yield significantly divergent outcomes over time, as it is already known. As before, an almost exact match can be observed between the FE MIFT 1-A S1, FE MIFT 2-A S1, and the Py-MIFT, especially in the medium and long

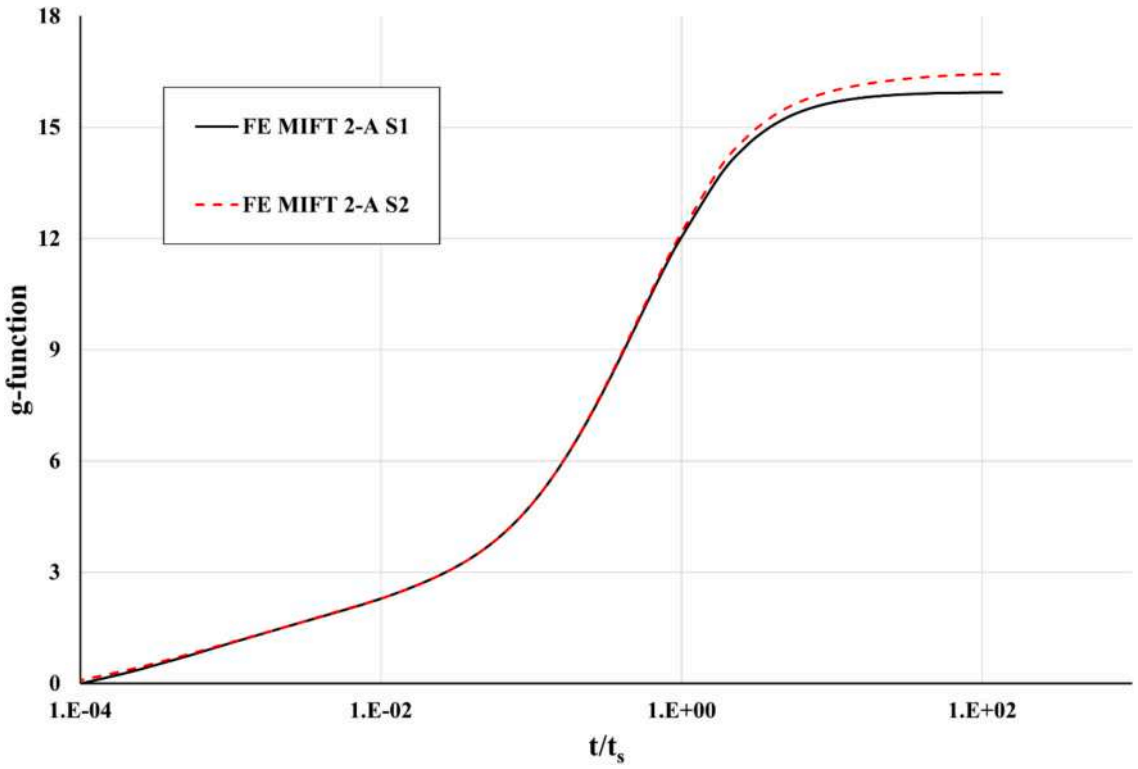

Fig. 16. Comparison of g-functions for the MIFT case obtained with COMSOL to investigate the impact of assuming uniform thermal properties and initial temperature.

term.

Neglecting the presence of the grout and modelling it with a constant resistance term has little impact in the long term, but impacts mainly in the short term, as known from the literature. The FE MIFT 2-A S1 model, which accounts for non-uniform borehole temperature, provides a more realistic representation than the simplified FE MIFT 1-A S1 model, which considers a uniform borehole temperature. This discrepancy primarily impacts the short-term thermal response, while the long-term outcomes remain comparable. Thus, the assumptions underlying the simpler models, including *pygfunction*, can be considered sufficiently accurate for long-term BTES system analysis.

In Fig. 15 the dimensionless g-functions obtained from simulations FE MIFT 2-A S1, FE MIFT 2-B S1, and FE MIFT 2-C S1 are shown. The curve obtained from FE MIFT 2-C S2, which models the extreme case of adiabatic upper condition, demonstrates the potential impact of upper insulation on the thermal response of these systems, both in the short and long term. In fact, this g-function exhibits a long-term maximum greater than 35 after 150 years. This value is the highest of all those obtained from the simulated cases. It is important to note that this value is non-dimensional and does not correspond to a temperature difference in degrees Celsius, but rather quantifies the cumulative thermal response of the system. This finding suggests an enhanced heat storage capacity of the medium under perfect insulation, underscoring the importance of properly accounting for the actual insulation conditions of the soil. However, the *pygfunction* library is unable to model an upper boundary condition of this nature or to take into account a layer of surface insulation. Consequently, the g-functions generated using this library may exhibit deviations when compared to those obtained with a FE model, which accurately represents the real conditions. As a result, *pygfunction* proves inadequate in this context due to its inability to account for the thermal effects of an upper insulation layer.

Moreover, a comparison between the FE MIFT 2-A S1 and FE MIFT 2-B S1 in Fig. 15 reveals that the real insulation layer currently installed in the SMARTEP BTES is not sufficiently effective in reducing heat losses to the external environment. This is not a modelling limitation, but rather a reflection of the actual thermal performance of the installed material. This limited effect is likely due to the modest thermal resistance of the insulation material, and to the relatively small difference between its thermal conductivity and that of the surrounding soil. As a result, the g-function corresponding to a BTES with such an insulation layer lies close to that of the uninsulated case and significantly below the fully adiabatic scenario. However, in general, the g-function of a BTES with an insulation layer of low thermal conductivity will lie between the two extremes of perfect insulation and bare soil.

As shown in Fig. 16, considering initial conditions and material properties that vary with depth does not result in a very dissimilar solution to that obtained by considering average values of these variables. The two g-functions slightly diverge only in the long term (the maximum of g-function from FE MIFT 2-A S1 is 16.43 compared to 15.93 for FE MIFT 2-A S2). In the context of a BTES, subjected to almost equal charge and discharge cycles over an extended period, this divergence becomes less relevant. From this perspective, *pygfunction* models can be considered sufficiently accurate when the used average constant thermal properties of materials are representative of realistic values. Even in this case, the use of FE models allows more realistic consideration of actual in-situ conditions.

5.3. Energy analysis results

As aggregation algorithms are required to reduce the computational load, errors are inevitably introduced. This is particularly evident in the context of solar-assisted BTES, where loads have significant seasonal variability. Various algorithms have been proposed in the literature, but almost none of them consider the actual load variations in their development.

In this work, three different aggregation algorithms were tested during a five-year simulation of the operation of the solar-assisted BTES. The analyses conducted indicated that the GAA is not suitable for a solar-

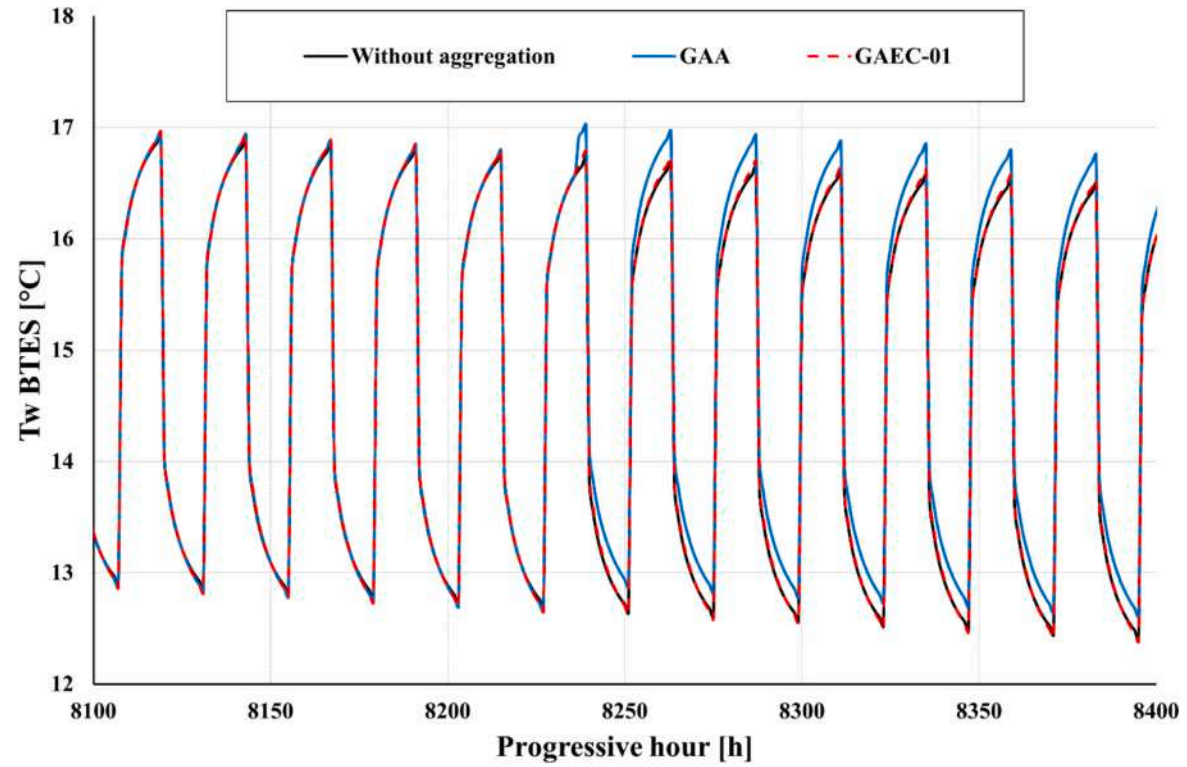

Fig. 17. Detailed view of the step error due to Geometric Aggregation at the end of the first simulated discharging phase (March 4–17), highlighting how the new algorithm effectively avoids these aggregation errors.

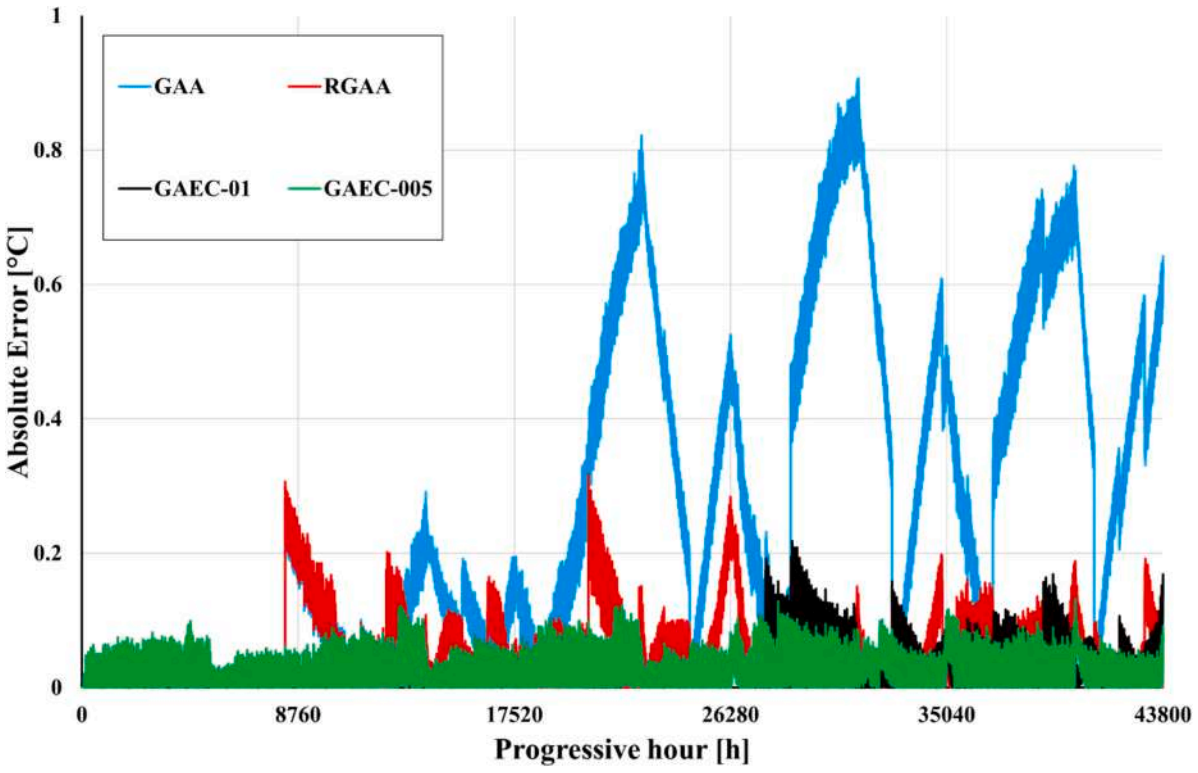

Fig. 18. Trend of Absolute Errors resulting from the comparison of the results obtained from the tested aggregation algorithm and the results obtained from a 5-year simulation without load aggregation.

assisted BTES, which is subject to highly variable loads during the year. This limitation becomes evident as early as the first year of the simulation. Fig. 17 shows the effect of aggregating the first 4096 h, incorporating positive and negative loads. The resulting aggregated load is almost zero and not representative of the previous load history. To mitigate this error, the RGAA was tested, which aggregates blocks of

Table 6
Error metrics (maximum AE and MAE) for the last year of a 5-year simulation, comparing the temperature profiles obtained using the tested load aggregation algorithm against the reference case without aggregation. The table also includes the corresponding computation times for each simulation.

Aggregation algorithms tested	Maximum AE	MAE	Computation Time
Reference (no aggregation)	–	–	1.53492×10^5 s
GAA	0.77 °C	0.42 °C	5.09×10^2 s
RGAA	0.19 °C	0.051 °C	5.57×10^2 s
GAEC-0.1	0.16 °C	0.038 °C	1.117×10^3 s
GAEC-0.05	0.13 °C	0.029 °C	1.142×10^3 s

2048 h at most, thereby reducing the number of hours of charging and discharging phase that can be aggregated. This algorithm has been demonstrated to contain the errors associated with unlimited aggregation, but even with RGAA, a step error is observed when aggregating 2048 h across charging and discharging phases, although the error is lower in absolute value over the long term. Within a year, both methods result in the same errors, as shown in Fig. 18. The new GAEC-0.1 proposed in this paper represents a significant advance in reducing the impact of aggregation errors. This new algorithm exhibits considerable enhancements since its implementation in the first year of simulation. Despite the slight increase in the computational load of the simulation, the introduction of errors is reduced, resulting in a smoother temperature trend without step errors (Fig. 17). The temperature calculated using this new load aggregation algorithm closely matches the

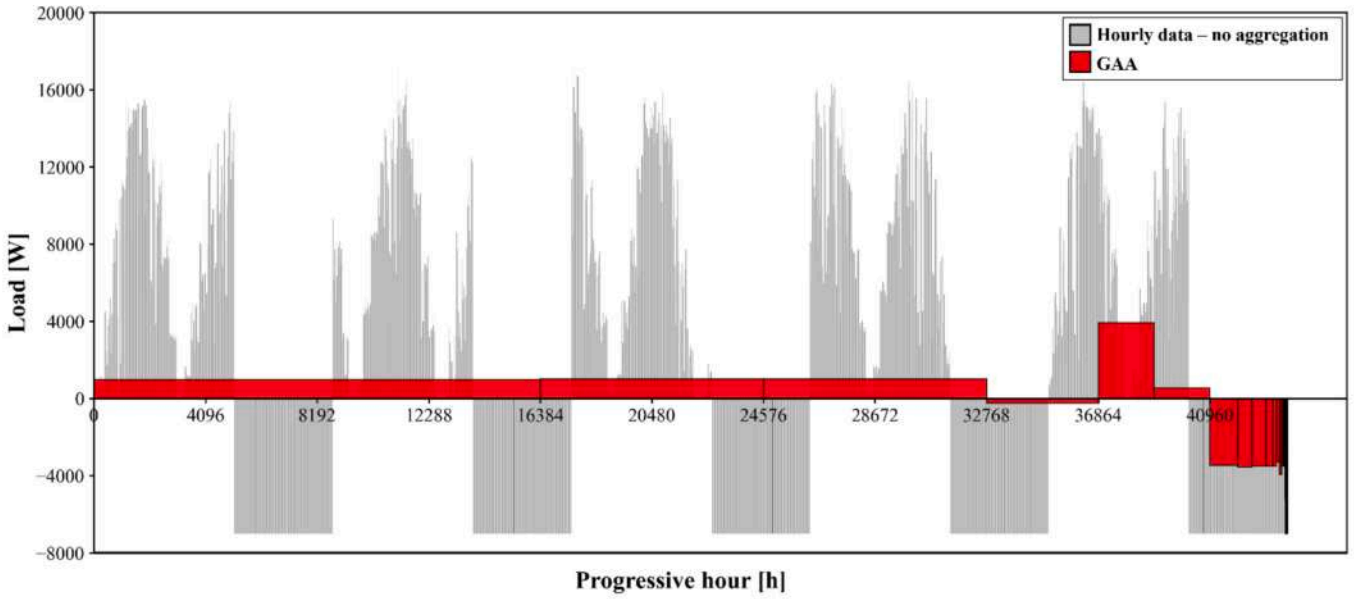

Fig. 19. Comparison of cumulative thermal loads (injected and extracted) between the Geometric Aggregation Algorithm (GAA), in red, and the non-aggregated profile (Hourly data), in grey, at the end of the fifth year of simulation.

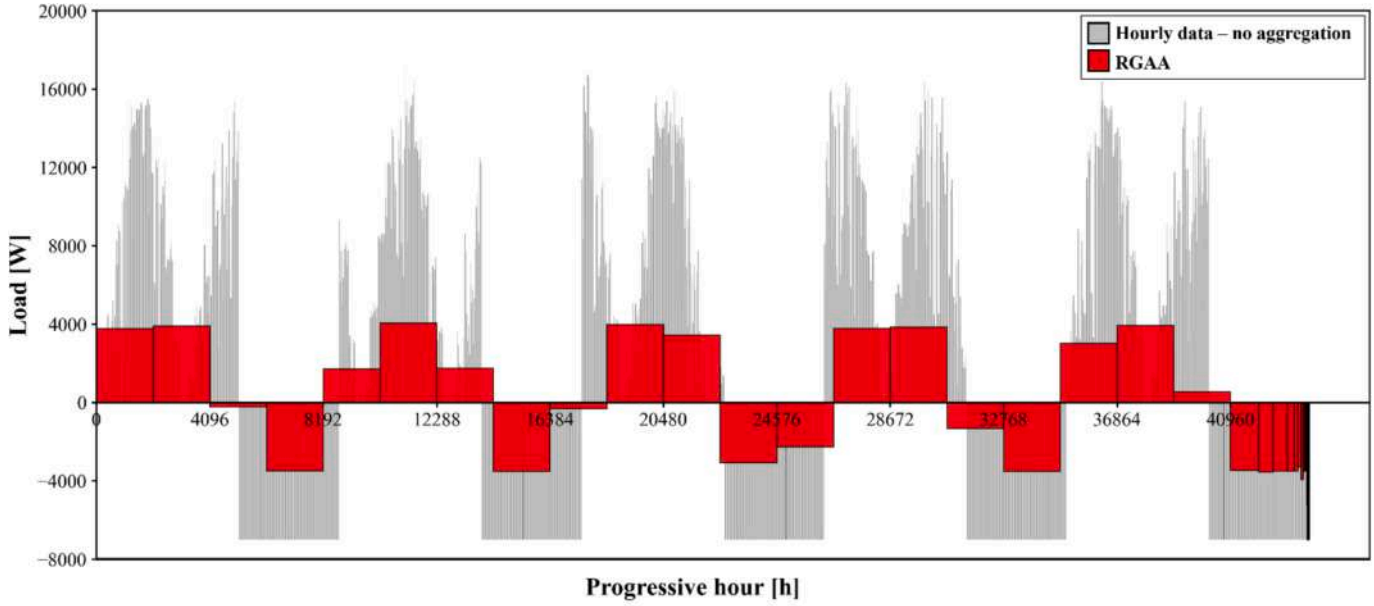

Fig. 20. Comparison of cumulative thermal loads (injected and extracted) between the Restricted Geometric Aggregation Algorithm (RGAA), in red, and the non-aggregated profile (Hourly data), in grey, at the end of the fifth year of simulation.

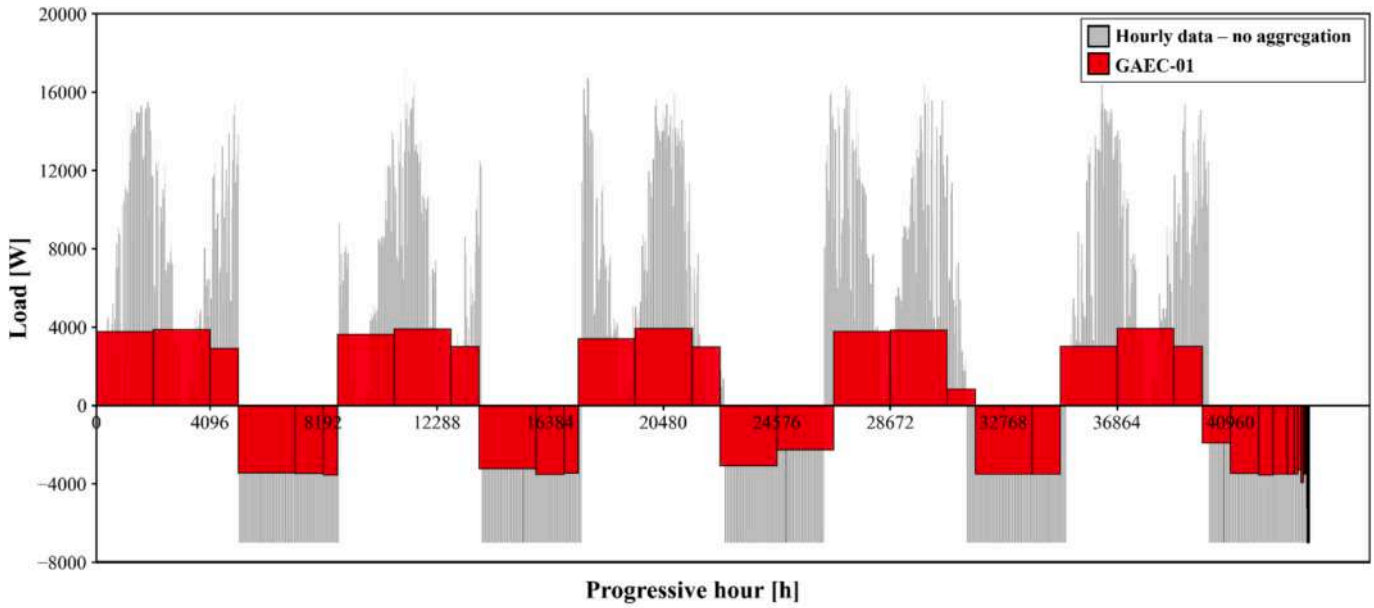

Fig. 21. Comparison of cumulative thermal loads (injected and extracted) between the new Geometric Aggregation with Error Control of 0.1 °C (GAEC-01), in red, and the non-aggregated profile (Hourly data), in grey, at the end of the fifth year of simulation.

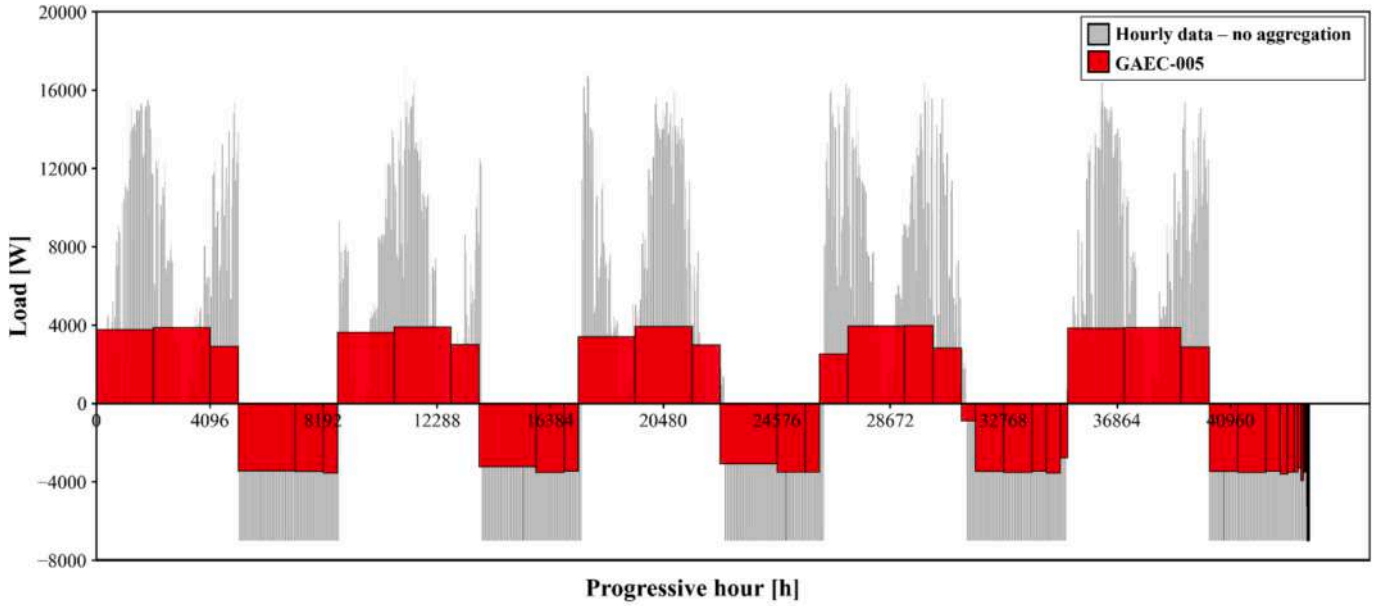

Fig. 22. Comparison of cumulative thermal loads (injected and extracted) between the new Geometric Aggregation with Error Control of 0.05 °C (GAEC-005), in red, and the non-aggregated profile (Hourly data), in grey, at the end of the fifth year of simulation.

temperature calculated without any aggregation.

Furthermore, the impact of the maximum permissible error was analysed by reducing the threshold value to 0.05 °C, with GAEC-0.05. The findings indicated a substantial increase in the computational load, which is significant when considering that only a small increase in long-term accuracy is achieved. As the error threshold decreases, the effect of the last loads on the fluid temperature becomes more significant. In order to observe a substantial improvement in the accuracy of the algorithm, the number of non-aggregated loads, currently set at 48 h, will have to be increased. These considerations can be deduced from the graph in Fig. 18, which shows the absolute errors resulting from the comparison of the aforementioned aggregation methods.

The performance of the various algorithms is illustrated in Fig. 18 where they are tested against the actual temperature obtained from the convolution product (Eq. (17), in the absence of any load history aggregation. The new algorithm outperforms the others, with absolute errors remaining mostly below 0.1 °C for GAEC-0.1 and below 0.05 °C for GAEC-0.05 over the simulated 5 years. This demonstrates that GAEC-0.05 delivers more accurate results, albeit at the cost of increased computational load. Table 6 shows the error metrics (maximum AE and MAE) calculated by comparing the temperatures obtained using the tested load aggregation algorithm with the reference temperatures obtained without any aggregation. The comparison refers to the final year of a 5-year simulation of the system's operation. The results highlight that the new algorithm achieves a maximum AE and a MAE an order of magnitude lower than those of the geometric aggregation algorithm.

Table 6 also reports the computation times for each simulation. For reference, the simulation without any aggregation required more than 1

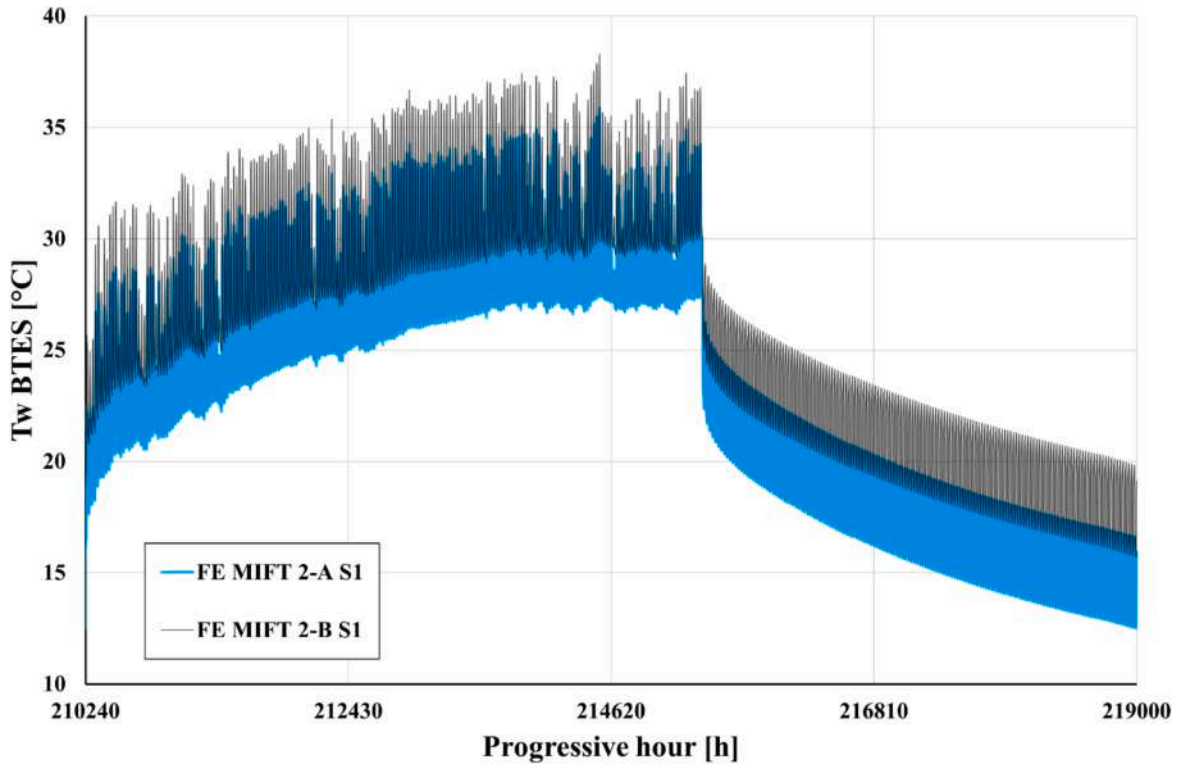

Fig. 23. 25th-year of the simulation for a solar-assisted BTES without an insulation layer and with a perfectly adiabatic surface.

day and 18 h, while the proposed GAEC-0.1 and GAEC-0.05 algorithms reduced this to 18 and 19 min, respectively. It is evident that the use of an aggregation algorithm is essential to reduce computational times. In the absence of the use of such an algorithm, computational times would be unmanageable.

Using an aggregation algorithm generally results in the attenuation of the original load distribution (as demonstrated in Figs. 19 to 22), except for the most recent loads. However, GAA and RGAA algorithms (see Figs. 19 and 20), despite being faster than GAEC-01 and GAEC-005 (see Figs. 21 and 22), show a tendency to oversimplify the original load distribution, resulting in inaccuracies, particularly during the transition between charging and discharging.

The algorithm developed and proposed in this work (GAEC-01 and GAEC-005), at the cost of a minor increase in computational expense, allows for a more realistic representation of seasonal load variations, as shown in Figs. 21 and 22, and reduce the errors introduced by the GAA and RGAA algorithms.

While GAEC-005 proves more accurate in reproducing the trend of hourly loads, it requires a higher computational effort compared to GAEC-01. For this reason, GAEC-01 was selected as a good compromise between speed and accuracy, offering reliable performance despite not being the most precise of the tested algorithms.

GAEC-0.1 was then used to perform a 25-year simulation considering a 20 m^2 field of Flat-Plate Collectors. As demonstrated in the graph presented in Fig. 23, the effect of insulation in terms of discharge water temperatures is not negligible (MAE = 2.79 °C for the final year of the 25-year simulation). In fact, at the end of the 25-year period, the temperatures returned by the BTES in FE MIFT 2-A S1 compared to FE MIFT 2-B S1 exhibit an Absolute Error up to 3.5 °C, highlighting the discrepancy introduced by neglecting the insulating layer in the model of the BTES.

However, at least for the case under study, the differences between the results obtained with the two models in terms of average annual storage efficiency (as defined in Eq. 16) are minimal, both amounting to approximately 68 %.

A broad comparison with the results reported in [31], where the same BTES system was coupled with a Road Thermal Collector and simulated using TRNSYS, further confirms the reliability of the newly developed Python model. In that study, an average seasonal storage efficiency of about $\eta_{BTES} = 75$ % was achieved over the first four years of operation. In the present work, the solar-assisted BTES configuration reaches an average efficiency of approximately $\eta_{BTES} = 68$ % (Eq. (16) over the first four years of operation, during which around $E_{injected} = 75$ MWh are injected and $E_{extracted} = 51$ MWh are extracted. Despite the differences in thermal sources and operating conditions, the similarity in efficiency values suggests a strong consistency between the two modelling approaches, even considering that the DST model implemented in TRNSYS does not allow for simulating a system layout exactly matching the one under investigation.

6. Conclusions

This study investigated the numerical modelling of the dynamic thermal response of solar-assisted BTES systems using various approaches based on g-functions. These g-functions were generated for a pilot BTES at the University of Palermo campus under several simplified physical assumptions. Python's *pygfunction* library and FE models developed in COMSOL Multiphysics® were used for g-function computation, and a new Python code was created to simulate the system's dynamic operation. Among the main contributions of this work is a novel load aggregation scheme that directly accounts for load variability. By applying an error threshold to control the maximum aggregation window, the algorithm accepts an aggregation step only if the induced temperature error remains below the chosen threshold. The new load aggregation scheme ensures that absolute errors in temperature remain consistently limited and within predictable limits, providing reliable results even under high load variability.

In the context of g-function generation, models based on a uniform heat transfer rate (UHTR) were employed to cross-validate the Python-based model against the FE model. The results demonstrated that the

g-functions derived from *pygfunction* and from FE simulations are practically superimposable, provided that the FE model's calculation domain has a radius of at least 20 times the conventional BTES radius (i.e., the radius of the circular surface containing all boreholes). Nonetheless, FE modelling proves more versatile for exploring complex boundary conditions. Subsequently, more complex models considering series and parallel connections (MIFT) were introduced to investigate the effects of different physical assumptions. Both the simplified and the more advanced MIFT models accurately captured the medium- to long-term borehole response. However, the simplified models led to errors in the short-term thermal response due to neglecting grout inertia, as previously noted in the literature. Furthermore, introducing variability in thermophysical properties and initial temperature had little effect on long-term behavior: after 150 years, the maximum g-function values were 16.43 and 15.94 with and without variability, respectively, indicating that a simplified approach can be sufficient for many applications. By contrast, upper insulation significantly influenced medium- to long-term performance: the MIFT g-function under a perfectly adiabatic boundary reached values around 35, substantially higher than in non-insulated or poorly insulated cases. The complete set of g-functions obtained from the developed models are provided as Supplementary Information.

These g-functions were then integrated into the Python-based code to simulate a system layout combining a 20 m^2 flat-plate solar collector field with a BTES system in Palermo. The results showed that the new algorithm enables explicit control over the error introduced by load aggregation, a feature not available in traditional methods. In the fifth year of the simulation, geometric aggregation resulted in a Mean Absolute Error (MAE) of 0.42 °C, with peak absolute error exceeding 0.8 °C, compared to non-aggregated reference simulations. By contrast, the new method with an imposed error threshold of 0.1 °C achieved a maximum absolute error less than 0.16 °C, with a significantly lower MAE of 0.038 °C. This represents an order of magnitude enhancement in accuracy compared to the conventional methods in this specific case of solar-assisted BTES systems.

Further simulations over a 25-year period compared perfectly adiabatic and non-insulated BTES configurations. The results revealed a 3.5 °C difference in long-term discharge water temperatures, emphasizing the critical role of insulation in sustaining storage performance. Additionally, the outcome in terms of storage efficiency (around 68 % annually) was consistent with those obtained using previous physical models for the same layout, thereby confirming the reliability of the new Python model.

Overall, the Python model incorporating the new aggregation algorithm will serve as the foundation for a digital twin of the Palermo pilot plant, facilitating real-time monitoring and control. Furthermore, future developments will include testing the algorithm on GSHP systems, which typically present non-symmetric thermal loads, to assess its applicability and robustness in different operational contexts.

CRediT authorship contribution statement

Angela Valeria Miceli: Writing – original draft, Visualization, Software, Methodology, Formal analysis, Conceptualization. **Alessandro Buscemi:** Writing – original draft, Investigation, Conceptualization. **Stefania Guarino:** Supervision, Software, Conceptualization. **Marco Beccali:** Methodology, Conceptualization. **Valerio Lo Brano:** Supervision, Conceptualization.

Declaration of competing interest

The authors declare that they have no known competing financial interests or personal relationships that could have appeared to influence the work reported in this paper.

Acknowledgements

This study was conducted as part of the research activities on borehole thermal energy storage systems within the Project "Network 4 Energy Sustainable Transition — NEST", Spoke 1: SOLAR: PV, CSP & CST, Spoke 8: Final use optimization, sustainability & resilience in energy supply chain, Project code PE0000021, Concession Decree No. 1561 of 11.10.2022 adopted by Ministero dell'Università e della Ricerca (MUR), CUP. Project funded under the National Recovery and Resilience Plan (NRRP), Mission 4 Component 2 Investment 1.3 - Call for tender No. 341 of 15.03.2022 of Ministero dell'Università e della Ricerca (MUR); funded by the European Union – NextGenerationEU. CUP B73C22001280006.

Appendix A. Supplementary data

Supplementary data to this article can be found online at https://doi.org/10.1016/j.enconman.2025.120666.

Data availability

Data will be made available on request.

References

[1] Record carbon emissions highlight urgency of Global Greenhouse Gas Watch n.d. https://wmo.int/media/news/record-carbon-emissions-highlight-urgency-of-global-greenhouse-gas-watch (accessed January 17, 2025).
[2] IRENA-International Renewable Energy Agency. World Energy Transitions Outlook: 1.5°C Pathway. World Energy Transitions 2023:1–176.
[3] Hannah Ritchie. Sector by sector: where do global greenhouse gas emissions come from? - Our World in Data. Published Online at OurWorldinDataOrg 2020. https://ourworldindata.org/ghg-emissions-by-sector (accessed January 10, 2025).
[4] Tracking Clean Energy Progress 2023 – Analysis - IEA. Paris: 2023.
[5] Space heating – Analysis - IEA. Paris: 2023.
[6] Mahon H, O'Connor D, Friedrich D, Hughes B. A review of thermal energy storage technologies for seasonal loops. Energy 2022;239:122207. https://doi.org/10.1016/J.ENERGY.2021.122207.
[7] Gonzalez-Ayala J, Blázquez CS, Lagüela S, Nieto IM. Assesment for optimal underground seasonal thermal energy storage. Energy Convers Manag 2024;308:118394. https://doi.org/10.1016/J.ENCONMAN.2024.118394.
[8] Lyden A, Brown CS, Kolo I, Falcone G, Friedrich D. Seasonal thermal energy storage in smart energy systems: District-level applications and modelling approaches. Renew Sustain Energy Rev 2022;167:112760. https://doi.org/10.1016/J.RSER.2022.112760.
[9] Lanahan M, Tabares-Velasco PC. Seasonal Thermal-Energy Storage: A Critical Review on BTES Systems, Modeling, and System Design for Higher System Efficiency. Energies 2017, Vol 10, Page 743 2017;10:743. 10.3390/EN10060743.
[10] Zhao X, Li Y, Chen X, Yin Y. Ten differences of seasonal borehole thermal energy storage system from ground-source heat pump system. Energ Buildings 2024;325:114994. https://doi.org/10.1016/J.ENBUILD.2024.114994.
[11] Chapuis S, Bernier M. Seasonal storage of solar energy in borehole heat exchangers 2009;11:599–606. 10.26868/25222708.2009.0599-606.
[12] Mitali J, Dhinakaran S, Mohamad AA. Energy storage systems: a review. Energy Storage Sav 2022;1:166–216. https://doi.org/10.1016/J.ENSS.2022.07.002.
[13] Renaldi R, Friedrich D. Techno-economic analysis of a solar district heating system with seasonal thermal storage in the UK. Appl Energy 2019;236:388–400. https://doi.org/10.1016/J.APENERGY.2018.11.030.
[14] Yuan X, Heikari L, Hirvonen J, Liang Y, Virtanen M, Kosonen R, et al. System modelling and optimization of a low temperature local hybrid energy system based on solar energy for a residential district. Energy Convers Manag 2022;267:115918. https://doi.org/10.1016/J.ENCONMAN.2022.115918.
[15] Guarino S, Buscemi A, Ciulla G, Bonomolo M, Lo BV. A dish-stirling solar concentrator coupled to a seasonal thermal energy storage system in the southern mediterranean basin: a cogenerative layout hypothesis. Energy Convers Manag 2020;222:113228. https://doi.org/10.1016/J.ENCONMAN.2020.113228.
[16] Panno D, Buscemi A, Beccali M, Chiaruzzi C, Cipriani G, Ciulla G, et al. A solar assisted seasonal borehole thermal energy system for a non-residential building in the Mediterranean area. Sol Energy 2019;192:120–32. https://doi.org/10.1016/J.SOLENER.2018.06.014.
[17] Lizana J, Ortiz C, Soltero VM, Chacartegui R. District heating systems based on low-carbon energy technologies in Mediterranean areas. Energy 2017;120:397–416. https://doi.org/10.1016/J.ENERGY.2016.11.096.
[18] Cimmino M. An approximation of the finite line source solution to model thermal interactions between geothermal boreholes. Int Commun Heat Mass Transfer 2021;127:105496. https://doi.org/10.1016/J.ICHEATMASSTRANSFER.2021.105496.

[19] Wang L. A simplified method for evaluating temperature effect on the behavior of layered soil with a time-varying cylindrical heat source. Soils Found 2022;62:101181. https://doi.org/10.1016/J.SANDF.2022.101181.
[20] Gao W, Qadrdan M. A composite analytical model to predict the thermal performance of borehole ground heat exchangers within stratified ground. Appl Therm Eng 2025;258:124668. https://doi.org/10.1016/J.APPLTHERMALENG.2024.124668.
[21] Luo Y, Cheng N, Xu G. Analytical modeling and thermal analysis of deep coaxial borehole heat exchanger with stratified-seepage-segmented finite line source method (S3-FLS). Energ Buildings 2022;257:111795. https://doi.org/10.1016/J.ENBUILD.2021.111795.
[22] Zayed ME, Shboul B, Yin H, Zhao J, Zayed AAA. Recent advances in geothermal energy reservoirs modeling: challenges and potential of thermo-fluid integrated models for reservoir heat extraction and geothermal energy piles design. J Energy Storage 2023;62:106835. https://doi.org/10.1016/J.EST.2023.106835.
[23] University of Wisconsin-Madison. Solar Energy Laboratory. TRNSYS, a transient simulation program. Madison, Wis.: The Laboratory n.d; 1975.
[24] Hellstrom G. Ground heat storage: Thermal analyses of duct storage systems. 1991.
[25] Ahmadfard M, Bernier M. A review of vertical ground heat exchanger sizing tools including an inter-model comparison. Renew Sustain Energy Rev 2019;110:247–65. https://doi.org/10.1016/J.RSER.2019.04.045.
[26] Eskilson P. Thermal analysis of heat extraction boreholes 1987.
[27] Yavuzturk C, Spitler JD. A Short Time step Response factor Model for Vertical Ground Loop Heat Exchangers. ASHRAE Trans 1999;105:475–85.
[28] Bernier MA, Pinel P, Labib R, Paillot R. A Multiple load Aggregation Algorithm for Annual Hourly Simulations of GCHP Systems. HVAC&R Res 2004;10:471–87. https://doi.org/10.1080/10789669.2004.10391115.
[29] Cimmino M. pygfunction: an open-source toolbox for the evaluation of thermal response factors for geothermal borehole fields. Proceedings of ESim 2018, the 10th Conference of IBPSA-Canada 2018.
[30] Cimmino M. Semi-Analytical Method for g-Function Calculation of bore fields with series- and parallel-connected boreholes. Sci Technol Built Environ 2019;25:1007–22. https://doi.org/10.1080/23744731.2019.1622937.
[31] Buscemi A, Beccali M, Guarino S, Lo BV. Coupling a road solar thermal collector and borehole thermal energy storage for building heating: first experimental and numerical results. Energy Convers Manag 2023;291:117279. https://doi.org/10.1016/J.ENCONMAN.2023.117279.
[32] Marcotte D, Pasquier P. Fast fluid and ground temperature computation for geothermal ground-loop heat exchanger systems. Geothermics 2008;37:651–65. https://doi.org/10.1016/J.GEOTHERMICS.2008.08.003.
[33] COMSOL Multiphysics®. www.comsol.com. COMSOL AB, Stockholm, Sweden. n.d.
[34] Yoon S, Lee SR, Xue J, Zosseder K, Go GH, Park H. Evaluation of the thermal efficiency and a cost analysis of different types of ground heat exchangers in energy piles. Energy Convers Manag 2015;105:393–402. https://doi.org/10.1016/J.ENCONMAN.2015.08.002.
[35] Kurevija T, Vulin D, Krapec V. Effect of borehole array geometry and thermal interferences on geothermal heat pump system. Energy Convers Manag 2012;60:134–42. https://doi.org/10.1016/J.ENCONMAN.2012.02.012.
[36] Guarino S, Lo Brano V, Kosny J. Understanding the transformative potential of solar thermal technology for urban sustainability. Front Sustainable Cities 2025;7. https://doi.org/10.3389/frsc.2025.1583316.
[37] Choi W, Kikumoto H, Ooka R. Critical comparison between thermal performance test (TPT) and thermal response test (TRT): differences in heat transfer process and extractable information. Energy Convers Manag 2019;199:111967. https://doi.org/10.1016/J.ENCONMAN.2019.111967.
[38] Buscemi A, Catrini P, Piacentino A, Cardona F, Munith KD. Energy-saving potential of ground source multiple chillers in simple and hybrid configurations for Mediterranean climates. Energy Convers Manag 2022;263:115721. https://doi.org/10.1016/J.ENCONMAN.2022.115721.
[39] Lanahan M, Tabares-Velasco PC. Seasonal Thermal-Energy Storage: A Critical Review on BTES Systems, Modeling, and System Design for Higher System Efficiency. Energies 2017, Vol 10, Page 743 2017;10:743. 10.3390/EN10060743.
[40] Cimmino M. g-Functions for fields of series- and parallel-connected boreholes with variable fluid mass flow rate and reversible flow direction. Renew Energy 2024;228:120661. https://doi.org/10.1016/J.RENENE.2024.120661.
[41] Davies JH, Davies DR. Earth's surface heat flux. Solid Earth 2010;1:5–24. https://doi.org/10.5194/SE-1-5-2010.
[42] Claesson J, Javed S. Explicit Multipole Formulas for Calculating Thermal Resistance of Single U-Tube Ground Heat Exchangers. Energies 2018, Vol 11, Page 214 2018;11:214. 10.3390/EN11010214.
[43] Lo Brano V, Orioli A, Ciulla G, Culotta S. Quality of wind speed fitting distributions for the urban area of Palermo. Italy Renew Energy 2011;36:1026–39. https://doi.org/10.1016/J.RENENE.2010.09.009.
[44] Liu Z, Yu Z (Jerry), Yang T, El Mankibi M, Roccamena L, Sun Y, et al. Experimental and numerical study of a vertical earth-to-air heat exchanger system integrated with annular phase change material. Energy Convers Manag 2019;186:433–49. 10.1016/J.ENCONMAN.2019.02.069.
[45] Feng Y, Gong D, Jiang S, Zhao L, Cui N. National-scale development and calibration of empirical models for predicting daily global solar radiation in China. Energy Convers Manag 2020;203:112236. https://doi.org/10.1016/J.ENCONMAN.2019.112236.